Summer 2016

A Comparison of Microstructure and Uniaxial Compressive Response of Ice-Templated Porous Alumina Scaffolds Fabricated from Two Different Particle Sizes

Nikhil D. Dhavale
Old Dominion University, ndhav001@odu.edu

Recommended Citation

Dhavale, Nikhil D.. "A Comparison of Microstructure and Uniaxial Compressive Response of Ice-Templated Porous Alumina Scaffolds Fabricated from Two Different Particle Sizes" (2016). Master of Science (MS), Thesis, Mechanical & Aerospace Engineering, Old Dominion University, DOI: 10.25777/mq9z-k622
https://digitalcommons.odu.edu/mae_etds/11

A COMPARISON OF MICROSTRUCTURE AND UNIAXIAL COMPRESSIVE RESPONSE OF ICE-TEMPLATED POROUS ALUMINA SCAFFOLDS FABRICATED FROM TWO DIFFERENT PARTICLE SIZES

by

Nikhil D. Dhavale
B.Eng., May 2008, University of Mumbai, India
M.B.A., August 2014, Webster University, MO

A Thesis Submitted to the Faculty of
Old Dominion University in Partial Fulfillment of the
Requirements for the Degree of

MASTER OF SCIENCE

AEROSPACE ENGINEERING

OLD DOMINION UNIVERSITY
August 2016

Approved by:

Dipankar Ghosh (Director)

Xiaoyu Zhang (Member)

Abdelmageed Elmustafa (Member)

ABSTRACT

A COMPARISON OF MICROSTRUCTURE AND UNIAXIAL COMPRESSIVE RESPONSE OF ICE-TEMPLATED POROUS ALUMINA SCAFFOLDS FABRICATED FROM TWO DIFFERENT PARTICLE SIZES

Nikhil D. Dhavale
Old Dominion University, 2016
Director: Dr. Dipankar Ghosh

Development of bio-inspired highly porous (>50 vol.%) cellular ceramics is crucial to meet the demand of high-performance lightweight and damage-tolerant materials for a number of cutting-edge applications including impact energy absorption, biomedical implants, and energy storage. A key design feature that is observed in many natural materials (e.g., nacre, bamboo, wood, etc.) is the presence of hierarchical microstructure that results in an excellent synergy of various material properties, which are otherwise considered as mutually exclusive in current paradigm of materials design. To this end, development of multilayered, interconnected and anisotropic cellular ceramics could benefit the aforementioned applications. However, mimicking natural design principles to develop robust cellular materials is of paramount challenge because most of the available processing techniques are limited to the fabrication of simple materials microstructures. In contrast, freeze casting is one emerging technique that has shown great promise to develop nature-inspired hierarchical cellular ceramics. While a large number of recent studies focused on the development of process-structure correlations of freeze-cast ceramics, understanding of the structure-property relationships has been extremely limited. Therefore, this thesis develops a custom-made unidirectional freeze casting device to investigate the effects of the variation of the particle size (0.3 μm vs. 0.9 μm) on the microstructure and uniaxial compressive response of ice-templated sintered alumina scaffolds as a function of solids loading and freezing front velocity (FFV). For comparable solids loading and FFV, particle size effects on the microstructure of the scaffolds are observed to be significant. Moreover, transition of the pore morphology with the increasing solids loading and FFV is observed to be more drastic for the scaffolds processed from the 0.9 μm particles compared to the 0.3 μm particles. Similarly, particle size variations also significantly influenced the relative density and porosity of the scaffolds. However, in spite of the observed differences of the microstructure, relative density and porosity, uniaxial compressive stress-strain measurements revealed marginal particle size effects on the compressive strength. The apparent marginal particle size effects on the compressive strength are rationalized based on the relative variation of the relative density, pore aspect ratio, and interlamellae bridge density in between the sintered alumina scaffolds processed from 0.3 μm and 0.9 μm particle sizes. This study also suggests that particle size variation within a range of submicrometer to few micrometers (typical particle size range used in ceramic processing) can be uniquely employed to systematically modify the microstructure of the ice-templated sintered ceramic scaffolds, without significantly altering their uniaxial compressive response; which can be useful to optimize the structure-property relationships of the ice-templated scaffolds for the structural, biomedical and functional applications.

DEDICATED TO ….

The four pillars of my life:

The Almighty GOD,

My beloved Parents,

My Teachers,

And,

My sweet little sisters,

For bestowing their seamless support and unrestricted love,

To achieve this success in my life.

ACKNOWLEDGMENTS

It brings me great pleasure to show my appreciation to all those who have helped me make this thesis research a success. First and foremost, I would like to express my sincere gratitude and heartfelt appreciation to my advisor Dr. Dipankar Ghosh, for his patience and enthusiasm throughout the course of this work. His technical expertise and invaluable guidance has helped me across the learning process of my research. Dr. Ghosh was always there to help me whenever I ran into trouble and has always steered me in the right direction. He has been a source of constant inspiration at every stage of my thesis research and writing, providing sound advice and good teaching. He is incredibly organized and a great mentor, which was of immense help in gearing my thesis forward. One simply could not wish for a better and friendlier supervisor.

I am gratefully indebted to my colleagues, Mr. Mahesh Banda and Mr. Hyungsuk Kang, for their valuable comments and engagement throughout the research and writing of this thesis. I also extend my sincere thanks to the staff in the Machine Shop at Old Dominion University as well as my lab mates Mr. Michael Beachy, Mr. Michael Harty, Mr. Michael Smith, Mr. John Simmonds and Mr. Joseph Hastings of the Senior Design Project team, for helping me build the customized experimental setup. You guys have great ideas and it was fun working with you all.

I would also like to acknowledge Dr. Xiaoyu Zhang and Dr. Abdelmageed Elmustafa, for agreeing to be on my thesis committee despite their busy schedules. Dr. Zhang has also helped by providing access to the high temperature box furnace for the sintering process. I also thank the Applied Research Center (ARC) of the College of William and Mary for providing the access to their desktop Scanning Electron Microscope (SEM).

I take this opportunity to express my appreciation to Dr. Sebastian Bawab for his kind support and encouragement throughout the thesis work, as well as Ms. Diane Mitchell for helping me in procuring all the required materials and supplies on time. I would also like to thank the Department of Mechanical and Aerospace Engineering for granting me permission to work on this research in their LEEM lab.

My parents have nurtured me in a very special manner, sculpting and steering my life at every stage with their continuous motivation and supervision. I would like to express my profound gratitude to my mother, my father, my teachers, my dear friends, and my sweet little angel sisters, who have been a source of unconditional support and encouragement throughout my life. I could not have come this far without their stimulation. To all of them, I dedicate this thesis.

Last but not the least, I would like to appreciate the Almighty GOD for providing me the strength, the courage, and the opportunity to attain this level. I extend my sense of gratitude to one and all, who has directly or indirectly, contributed to the success of this thesis.

Thank you all very much.

NOMENCLATURE

ABBREVIATIONS

FFV	Freezing Front Velocity
SA	Sub-micrometer size Alumina powder particles (0.9 μm)
NA	Nanometer size Alumina powder particles (0.3 μm)
Al_2O_3	Alumina (Aluminum Oxide) powder
α-Al_2O_3	α-phase (crystalline polymorphic phase) of Alumina
SEM	Scanning Electron Microscope
L-N_2	Liquid Nitrogen

ROMAN SYMBOLS

T_g	Glass transition temperature
t	Lamella thickness
a	Major axis of the pore
b	Minor axis of the pore
p_t	Total porosity of the cellular solid
v_c	Critical freezing front velocity
a_O	Average intermolecular distance
d	Thickness of the film
R	Radius of the particle
z	Exponential constant

GREEK SYMBOLS

ρ_r	Relative density of the cellular solid
ρ^*	Apparent density of the cellular solid
ρ_s	Density of the constituent material
μ	Interlamellae spacing/wavelength
χ_p	Pore aspect ratio
ρ_b	Lamellae bridge density
$\Delta\sigma$	Mean free energy of the particle
η	Viscosity of the suspension
$\rho_{b(SA)}$	Average lamellae bridge density of submicron Al_2O_3 scaffolds
$\rho_{b(NA)}$	Average lamellae bridge density of nano Al_2O_3 scaffolds

TABLE OF CONTENTS

Page

Chapter

LIST OF TABLES

Table Page

LIST OF FIGURES

CHAPTER 1

INTRODUCTION

There is a significant demand for novel cellular ceramics (porosity >50 vol.%) with improved mechanical properties for armor systems, aircraft structures, automobiles bumpers, biomedical implants, and energy storage. It is also desirable that such novel porous architectures can be fashioned into bulk complex shapes and are easy to scale-up with low manufacturing cost. In spite of several well-established techniques available to fabricate cellular ceramics, resulting porous architectures exhibit limitations to meet the demand of the aforementioned applications. Natural materials such as bone, wood, and seashells supported technological developments at the early stages of humanity, but were eventually replaced by the engineering materials. However, we are still fascinated by the elegant hierarchical design architectures observed in natural solids leading to unprecedented properties and yet to incorporate natural design principles in the current practice of materials engineering to design robust materials and devices. This has generated much of the current interest in biostructure-enhanced material design and manufacturing. However, mimicking the structural features of the natural solids that vary with the length-scale is not a trivial undertaking.

A striking microstructural feature of many natural cellular materials is the presence of a multilayered, interconnected, and anisotropic pore morphology. Experimental and numerical investigations on natural cellular solids suggest that such anisotropic pore architecture could be beneficial to improve the mechanical and functional properties of engineering cellular solids. To this end, freeze casting (also known as ice-templating) has emerged as one promising technique that is capable of producing hierarchical multilayered structures containing oriented pores similar to that observed in the natural solids. It is also a cost effective and environment friendly powder processing technique. To explore the potential of the freeze casting technique, numerous investigations have been conducted so far that focused primarily on the processing of various ceramic materials and understanding the inherent physics of the process to ultimately establish the processing-microstructure relationships. It is of note that the majority of the deemed applications of freeze-cast cellular ceramics require to operate the materials under load-bearing conditions. Therefore, it is essential to develop deeper understanding of the influence of the processing and materials variable on the mechanical response of freeze-cast ceramics. However, development of the process-structure-property (mechanical in particular) relationships has been extremely limited. It is also of note that currently there is no commercial set-up available that can be directly employed to fabricate freeze-cast cellular ceramics.

Therefore, purpose of this thesis is twofold: (i) to develop a custom-made freeze casting set up that allows the fabrication of cellular ceramics under an applied unidirectional temperature gradient (i.e., unidirectional freezing conditions) and (ii) to compare the microstructure and uniaxial compressive response of ice-templated alumina ceramics processed from two different particle sizes to shed some light into the structure-property (mechanical) relationships. The structure of this thesis is as follows. In Chapter 2, a brief summary of the commonly utilized cellular ceramics fabrication techniques is provided followed by the discussion on the fundamental principles of the freeze casting technique. Chapter 3 describes the development of the custom-made unidirectional freeze casting set up and the processing steps that are involved in the fabrication of ice-templated cellular ceramics. Finally, Chapter 4 discusses the results of an experimental investigation that compares the microstructure and uniaxial compressive response of ice-templated alumina ceramics as a function of the solids loading of aqueous suspensions and freezing front velocity. This thesis concludes with the suggestions for the future work that will provide further insights into the process-structure-property relationships of freeze-cast cellular ceramics.

CHAPTER 2

LITERATURE REVIEW

2.1 CELLULAR SOLIDS, PROPERTIES AND APPLICATIONS

Dense materials processed by powder metallurgical routes usually contain defects in the form of pores or voids. Porosity, in general, is not desirable in engineering solids because of the detrimental effects on the mechanical and functional properties in the end applications [1]. However, most of the engineering solids such as metals, ceramics, and polymers contain small percentages of processing-induced porosity which is inevitable. Interestingly, there are numerous natural solids such as bones, cork, wood, leaves, sponges, and coral where the constituent materials are arranged in a fashion that lead to the formation of a two or three dimensional arrangement of pores creating highly porous architectures. The superior structural and biological functionalities of such natural porous solids are attributed to a combination of both, the constituent material(s) and the porous structure. As the nature continues to inspire the development of the modern materials and structures, engineered cellular solids emerged as a special class of materials with unique structures that contain a specific arrangement of the micro/macroscopic pores and a porosity level of 30 vol.% or higher [2, 3].

Both natural and engineered cellular solids find extensive use as in lightweight structures, load-bearing components, thermal insulations, filters, packaging materials, solid-state battery electrodes, solid oxide fuel cells, and impact energy absorbing structures. The low density of cellular solids aids in designing lightweight but mechanically tolerant structures such as sandwich panels that are widely used in automobile, aerospace and military applications. The low thermal conductivity of cellular solids facilitates the fabrication of reliable, efficient, and economical thermal insulations that can only be matched in performance by expensive vacuum-based insulations. Cellular solids typically undergo progressive failure at a relatively constant stress and exhibit large compressive strain before complete densification, making them ideal structures for high energy-absorbing applications under impact loading conditions [3]. Due to high damping capacity, cellular solids are utilized in electron microscope laboratories, theaters and auditoriums for protection from surrounding noise and vibrations. Cellular solids are also useful in minimizing the attenuation of electromagnetic waves for instance in radio transmitters. There are also numerous domestic and industrial applications of cellular solids for filtration of water, hazardous chemicals, molten metals, etc. [3].

Structurally engineered cellular solids can be broadly categorized into honeycombs and foams. Typical porous honeycomb structure consists of two-dimensional array of hexagons/polygons that are elongated along the third dimension, similar to that observed for the hexagonal cells of the bee-hive. Therefore, the honeycomb cellular architecture is characterized by the long and parallel pores, which are separated by the cell walls (Fig. 2.1a) [3]. On the other hand, foams are cellular solids containing polyhedral shaped cells that are packed in three dimensions to occupy the entire available space. Foams can be fabricated as both open-cell (Fig. 2.1b) and closed-cell structures

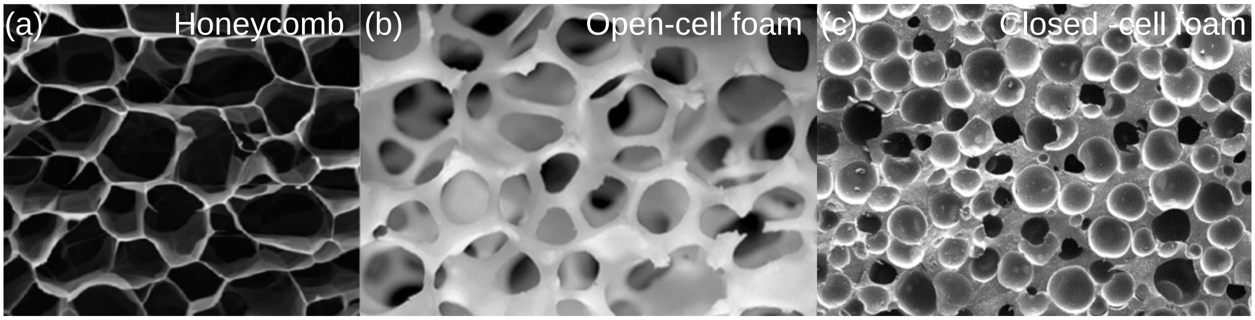

Figure 2.1: Representative microstructures of (a) honeycomb [4], (b) open-cell foam [5] and (c) closed-cell foam [6].

(Fig. 2.1c). If the constituent material of the foam is contained only in the cell edges, then the foam is said to be an open-cell foam [3]. If the edges and the faces are both solid, so that each cell is isolated from its adjacent cells, the foam is said to be a closed-cell foam. Typically, cellular solids are considered as structures and most of the available materials can be processed into cellular solids possessing a porous architecture.

As a result, cellular solids have been fabricated from various metals, ceramics, polymers, and composites. For example, clay (alumino silicates), alumina (Al_2O_3), silicon carbide (SiC), partially stabilized zirconia (ZrO_2), titania (TiO_2), silica (SiO_2), and glass are commonly employed materials that are utilized for the fabrication of open-cell and closed-cell ceramic foams [7-11]. Properties of foams and honeycombs are influenced by three factors: (i) relative density ($\rho_r = \rho^*/\rho_s$), where ρ^* and ρ_s are the apparent density of the cellular solid and constituent material, respectively, (ii) properties of the solid of the cellular solid is made, and (iii) the topology (connectivity) and shape of the cells [3, 12]. Variation of the ρ_r, constituent material, pore morphology and connectivity strongly affect the properties of cellular solids. Total porosity (p_t) of cellular solids is estimated as $p_t = (1 - \rho_r) * 100$. Since the load-bearing capacity of cellular solids is crucial for majority of the applications, their mechanical response of cellular solids has been investigated extensively. Figure 2.2 shows the representative uniaxial compressive stress-strain curves of cellular solids as well as the critical parameters such as the stiffness (slope of the linear part of the stress-strain curve), peak stress, plateau stress, densification strain, and total energy absorption (area under the stress-strain curve up to densification strain), which are extremely important to understand the load-bearing characteristics of porous structures. For each stress-strain curve, three distinct zones can be observed that are characteristics of cellular solids [3, 13-16]: (i) an elastic region where stress increases almost linearly with strain, (ii) a plateau

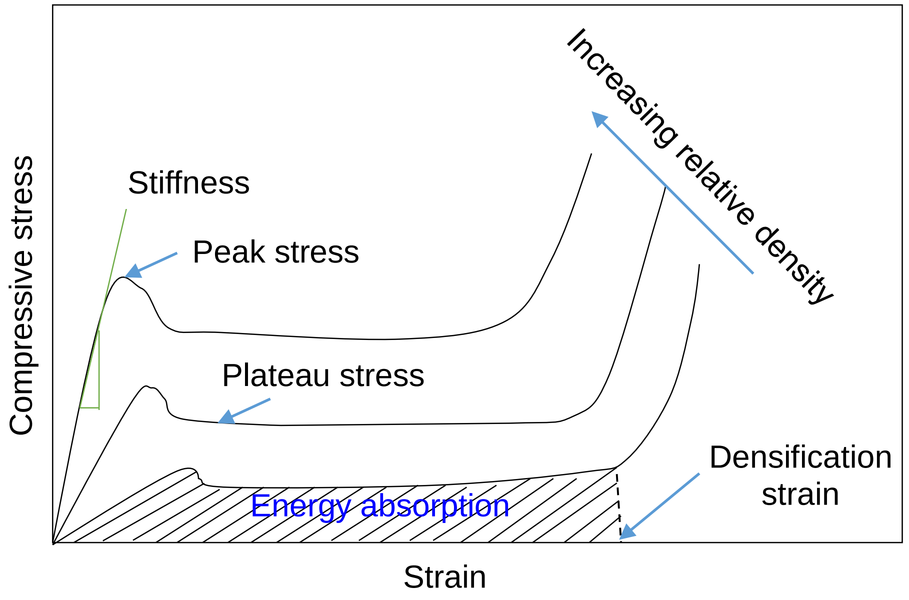

Figure 2.2: A Schematic of uniaxial compressive stress – strain curves of cellular solids with different relative densities.

region where deformation proceeds almost at a constant stress level (plateau stress) up to a large strain value, and (iii) a densification stage where further compression results in a steep rise of stress with strain. As the material is loaded, stress reaches a peak value (peak stress) and a slight drop in the stress is observed that is almost maintained in the plateau region (plateau stress). In cellular solids, peak stress is one key property indicative of the resistance to the initiation of inelasticity and corresponds to a stress level where failure begins in the structure. The plateau region is associated with a continued crushing and collapse of the cellular structure, and this process is primarily attributed to the energy-absorbing ability of the cellular solids. Stiffness, peak stress, plateau stress, and densification strain are strongly influenced by ρ_r. In general, stiffness, peak stress, and plateau stress increase with increasing ρ_r whereas the densification strain shows an inverse relationship with ρ_r (Fig. 2.2). Such variations with ρ_r also significantly affect the energy absorption capacity of cellular solids.

While the choice of material system for a specific application is often less critical, developing cellular solids with the desired microstructure and properties is extremely challenging. This is because for a given material system and porosity, properties are significantly influenced by the type of porosity (open-cell vs. closed-cell), pore connectivity, pore size and morphology, cell wall structure, and pore anisotropy. For example, closed-cell foams typically exhibit better mechanical and thermal properties relative to open-cell foams. Similarly, anisotropic cellular solids exhibit improved properties in comparison to isotropic porous solids. Therefore, the fabrication of cellular solids is a complex topic and there is no single processing technique that can address all the microstructure variables which control their properties and performance. As a result, numerous processing techniques have evolved to develop a wide variety of cellular solids with different micro-/macrostructures and thus properties. A brief description of various techniques employed for the fabrication of cellular solids is provided further. However, the discussion here is limited to only few techniques that are commonly employed to fabricate cellular ceramics.

2.2 FABRICATION OF POROUS CERAMICS

Initially, cellular ceramics have been processed by partial sintering of loosely packed ceramic powder compacts, which mainly leads to the formation of open-cell porous materials. However, such process yields porous ceramics with low porosity (less than 60 vol. %) and microstructure control remains very limited. Eventually, several techniques have been developed that can fabricate cellular ceramics with controlled microstructures and greater level of porosity, thus making it possible to develop tailored porous ceramics that can meet the demand of a specific application [17-20]. In general, cellular ceramics fabrication techniques can be classified into six categories: (i) replica method, (ii) direct foaming, (iii) sacrificial phase technique, (iv) paste extrusion, (v) amorphous bubble bonding (ABB), and (vi) rapid prototyping. In the following, a brief description of the above six techniques is provided.

2.2.1 Replica Method

In the replica method (also called polymeric sponge technique), an open-cell polymeric foam/sponge is immersed within a ceramic suspension to apply a ceramic coating on the surfaces of the foam [19]. This is followed by a pyrolysis process (heat treatment) to burn off the polymer component, which leaves behind a ceramic skeleton and is next sintered to develop a porous ceramic structure that is a replica of the starting polymeric foam [21]. Figure 2.3 shows a schematic of the replica method illustrating the steps involved in the fabrication of ceramic foams [19]. A typical ceramic foam microstructure obtained through the replica method is shown in Fig. 2.4 [22].

A general requirement is that the ceramic suspension should have a low enough viscosity so that it can penetrate well into the porous structure of the polymeric foam and a uniform coating can be achieved which should be able to replicate the surface details of the foam. In general, ceramic

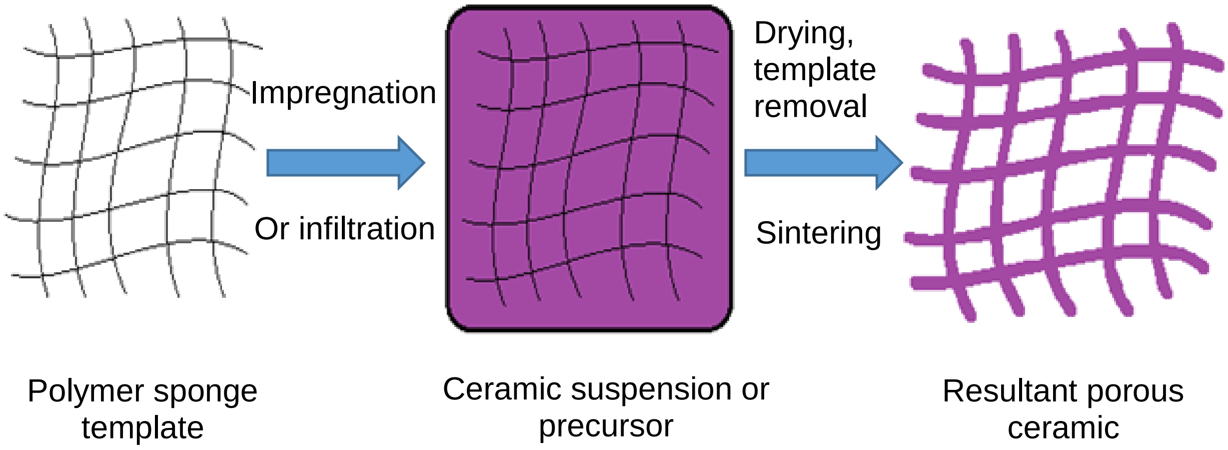

Figure 2.3: A schematic of the replica method illustrating all the steps involved in the fabrication of a ceramic foam [19].

foams, derived through the replica method, have a high permeability due to open-cell morphology with large pore size (ranging from 200 μm to 3 mm) and high porosity, which however, limit the mechanical performance of the foams [19, 21, 23]. Overall, due to simplicity and limited number of steps involved in the processing as well as availability of polymeric foams/sponges with well-controlled micro/macro-structures, the replica method is widely utilized to develop various commercial cellular ceramic products such as the Al_2O_3 and SiC filters employed for the wastewater treatment.

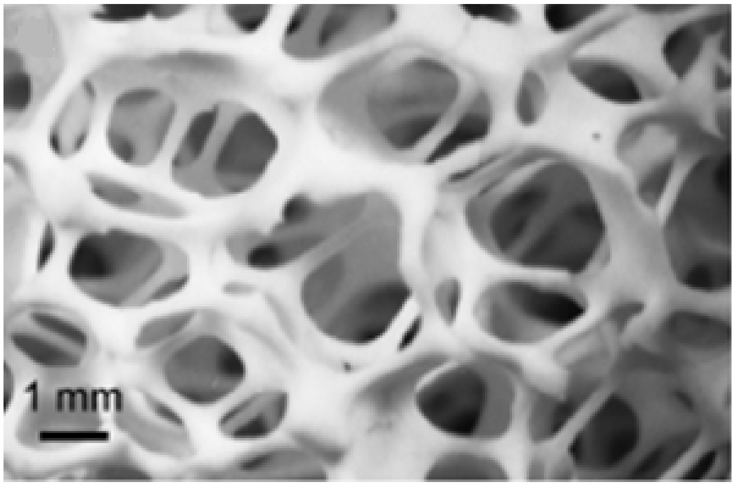

Figure 2.4: Microstructure of Al_2O_3 open-cell foam fabricated using the replica method [22].

2.2.2 Direct Foaming

In the direct foaming technique, a ceramic suspension is first foamed by introducing gas bubbles into the suspension. Next, the suspension is polymerized to retain the porous architecture induced through the gas bubbles, followed by demolding, drying, and sintering in order to develop a porous ceramic structure. Finally, the sintered foams are glazed to improve the mechanical properties of

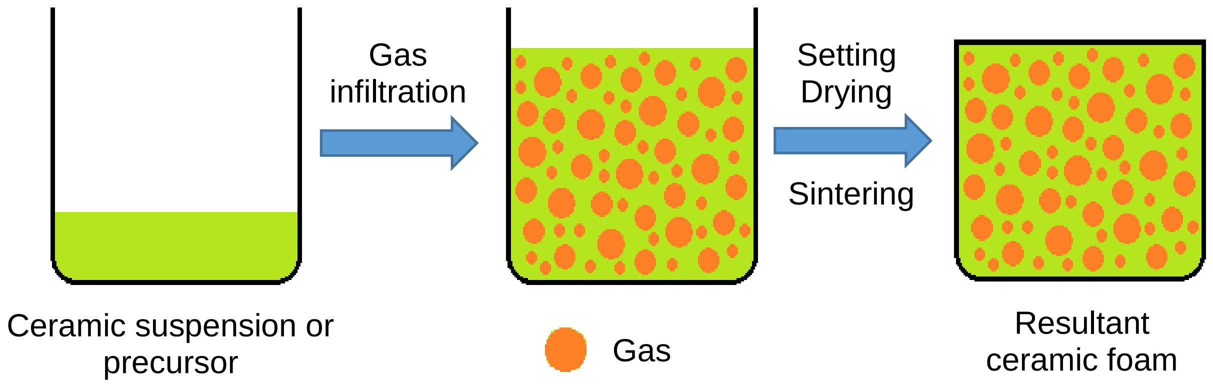

Figure 2.5: A schematic representation of the direct foaming technique [19].

the porous ceramics. Figure 2.5 schematically shows the various steps of the direct foaming technique. In general, this technique can produce highly porous green bodies that are relatively stronger and can withstand the force during machining [19]. Porosity of the resultant foams depends directly on the amount of the gas supplied into the suspension during the foaming process, whereas the pore size is dictated by the stability of the wet foam. Two different methods are employed for the stabilization of the wet foam. One utilizes biomolecules such as proteins, lipids, and surfactants, which are adsorbed on the surfaces of the gas bubbles thereby decreasing the interfacial energy between gas and media, thus preventing the coalescence of the gas bubbles. However, the stabilization through surfactants lasts only for several minutes whereas proteins stabilization can last for several hours. The other effective method to stabilize the wet foam is to utilize ceramic particles with a modified surface chemistry to enhance the ability of the particles to adsorb the long-chain amphiphilic molecules on the surface. Such process has been observed to stabilize the foamed ceramic suspensions for several days [2]. Figure 2.6 shows typical microstructures of ceramic foams developed using the direct foaming technique [22-24]. The direct foaming technique provides a relatively fast and environmental-friendly way to produce cellular

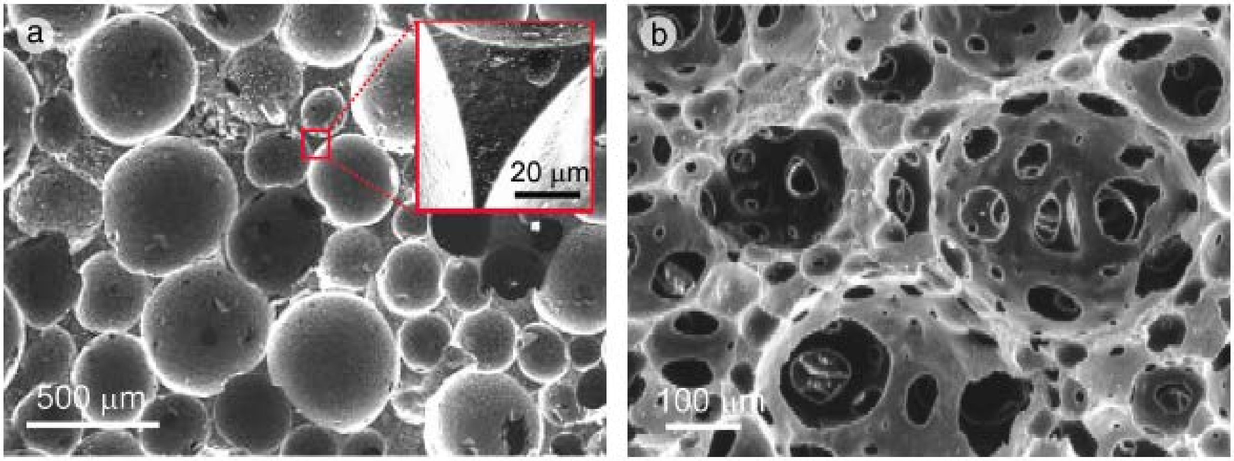

Figure 2.6: Representative microstructures of (a) closed-cell and (b) open-cell ceramic foam fabricated employing the direct foaming technique [22–24].

ceramics with a wide range of porosity. Due to defects-free cell struts, cellular ceramics fabricated by the direct foaming technique tend to be relatively stronger in comparison to the foams fabricated by the replica method [19].

2.2.3 Sacrificial Phase Technique

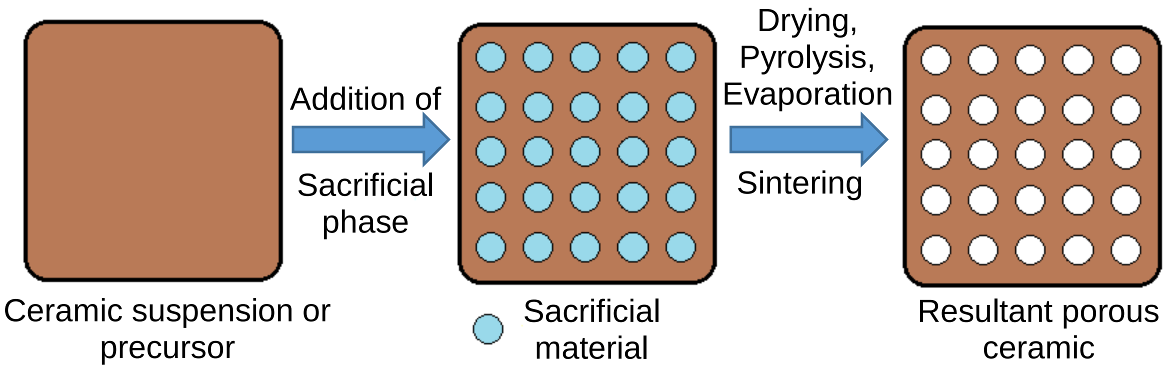

Figure 2.7: A schematic representation of the sacrificial phase technique [19].

The sacrificial phase technique for the fabrication of porous ceramics involves the preparation of a two-phase composite consisting of a continuous matrix of ceramic and a sacrificial particulate phase [19]. To obtain a two-phase composite mixture the sacrificial phase is first homogeneously mixed with the ceramic powder or its precursor(s). Homogeneous dispersion of the sacrificial phase within the matrix is a critical step to develop a uniform porous structure. The sacrificial phase is next removed from the mixture by pyrolysis, sublimation or evaporation, followed by sintering to obtain the final porous ceramic structure. The final porous structure is thus a negative replica of the initial sacrificial phase, as opposed to a positive cellular structure that is achieved in the replica method [20]. A schematic of the overall process is depicted in Fig. 2.7, and Fig. 2.8 shows the typical porous microstructures develop using the sacrificial phase technique [25-28]. The following routes are employed to develop the two-phase preform that after pyrolysis (or sublimation/evaporation) and sintering leads to the final porous structure: (i) dry mixing of the component phases followed by pressing [29], (ii) forming a two-phase colloidal suspension followed by slip, tape or direct casing [30], and (iii) impregnation of a previously consolidated

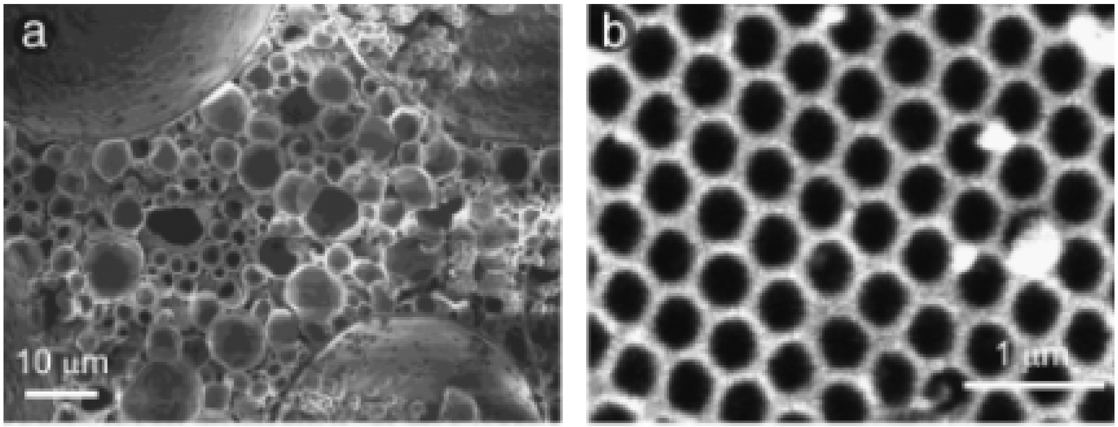

Figure 2.8: Microstructures of macroporous ceramics produced using the sacrificial template method: (a) a TiO_2 foam [25] and (b) an ordered macroporous SiO_2 foam [26].

preform of the sacrificial material with a pre-ceramic phase or a ceramic suspension [31]. A wide variety of materials such as the starch, wax, water, oil, gelatin, cellulose, sucrose, nylon, PVC, PS, PMMA, PVB, and naphthalene are utilized as the pore forming agents [19]. By proper selection of the sacrificial phase, it is possible to vary the pore size from 1-700 μm and total porosity from 20-90 vol. %. Since the final porous structure is a negative replica of the sacrificial phase, defects in the ceramic walls can be avoided resulting in improvement of the mechanical strength of the porous ceramics [19].

2.2.4 Paste Extrusion

Paste extrusion is a conventional technique generally employed to manufacture honeycombs mainly used for catalysts and filters. In this technique, a paste of ceramic powder, binders, and a lubricating agent is prepared using high-shear mixing. An extrusion ram forces the paste through a die and results in an extruded product of a desired shape, which can be further molded into

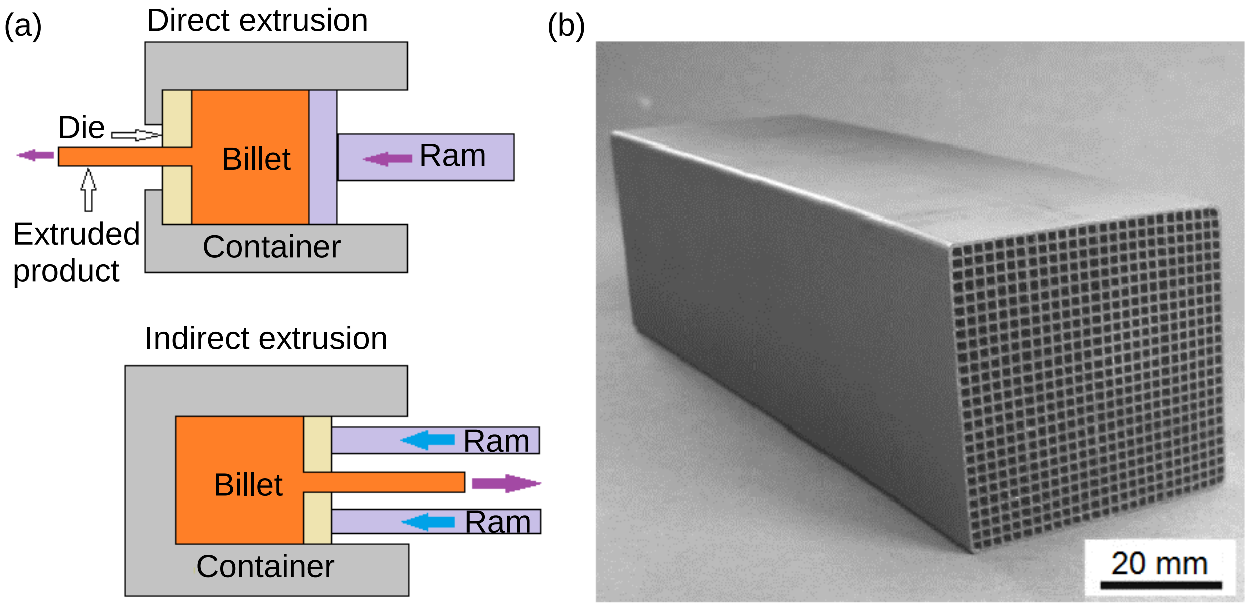

Figure 2.9: (a) A schematic of the extrusion process and (b) a honeycomb structure produced using the process [2].

required shape and length. A schematic of the paste extrusion process in shown in Fig. 2.9a. Next, the extruded green bodies go through a typical ceramic processing route of drying, binder burn-out, and sintering to produce the final macro porous ceramics [2]. The main advantage of this technique is that, the honeycomb porous structures can be extruded with unidirectional channels of desired cross-sectional shapes such as square, circular, and triangular [32]. Figure 2.9b shows a honeycomb structure produced using the paste extrusion process.

2.2.5 Amorphous Bubble Bonding (ABB)

A relatively less explored but unique cellular solid fabrication technique is where hollow spheres can be bonded together by applying heat to a cellular network of precursor hollow spheres [33,34], as shown in Fig. 2.10. Recently, amorphous bubble bonding (ABB) technique has been utilized to develop silicate glass-based cellular solids that involves heating hollow spheres of aluminosilicate glass (glass bubbles, diameters ranging from 10 to 100 μm) above the glass transition temperature (T_g), where the glass bubbles thermally bond to form a cellular structure through viscous flow and

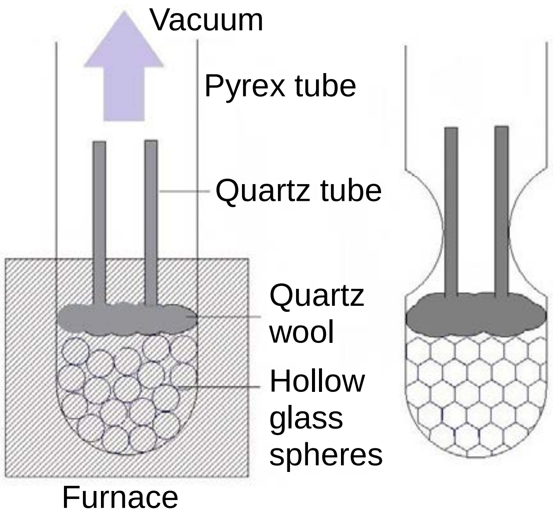

Figure 2.10: A schematic of foam fabrication using amorphous bubble bonding (ABB) technique [35].

deformation [35]. This technique can be employed to material systems such as bulk metallic glasses (BMGs), polymers, ceramics and glasses having sufficient thermal stability above T_g.

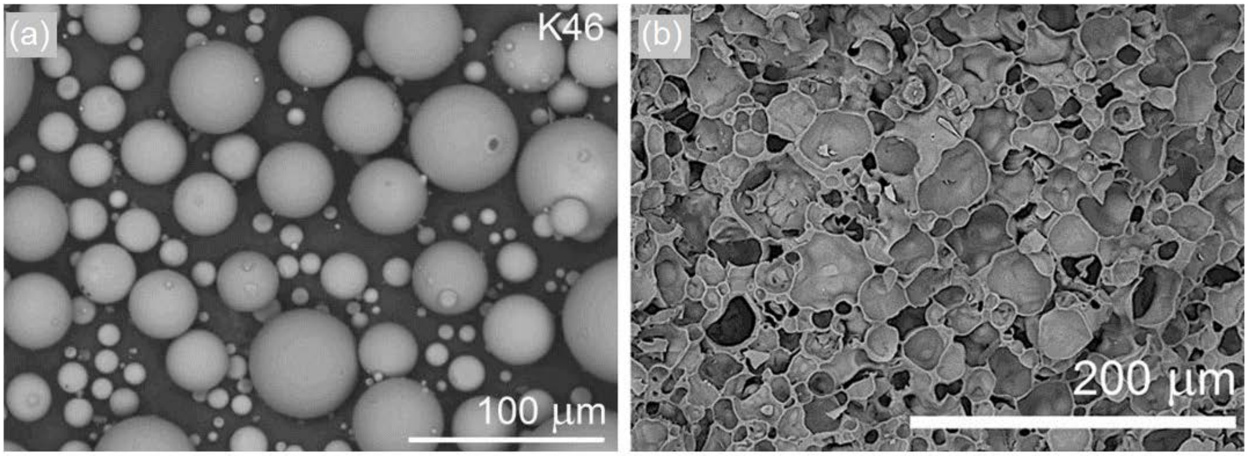

Figure 2.11: (a) SEM micrograph of the hollow K46 glass microspheres and (b) microstructure of the glass foam produced using the ABB technique [36].

Typically, ABB results in a predominantly closed-cell pore morphology, which is governed by the properties of the glass bubbles and the processing parameters. Figure 2.11 shows the SEM micrograph of the hollow K46 glass microspheres and microstructure of the glass foam produced using the ABB technique [36].

2.2.6 Rapid Prototyping Technique

Rapid Prototyping (RP) technique, also known as solid free-form fabrication is employed to produce a scaled or full-sized prototype from complex datasets, in which, three-dimensional (3D) objects are assembled by point, line or planar addition of the material [37]. Molds or dies which usually carry the ceramic suspension are not required in this processing route. [37]. A number of RP techniques are currently commercially available including stereolithography (SLA) [38], selective laser sintering (SLS) [39], laminated object manufacturing (LOM) [40-41], fused

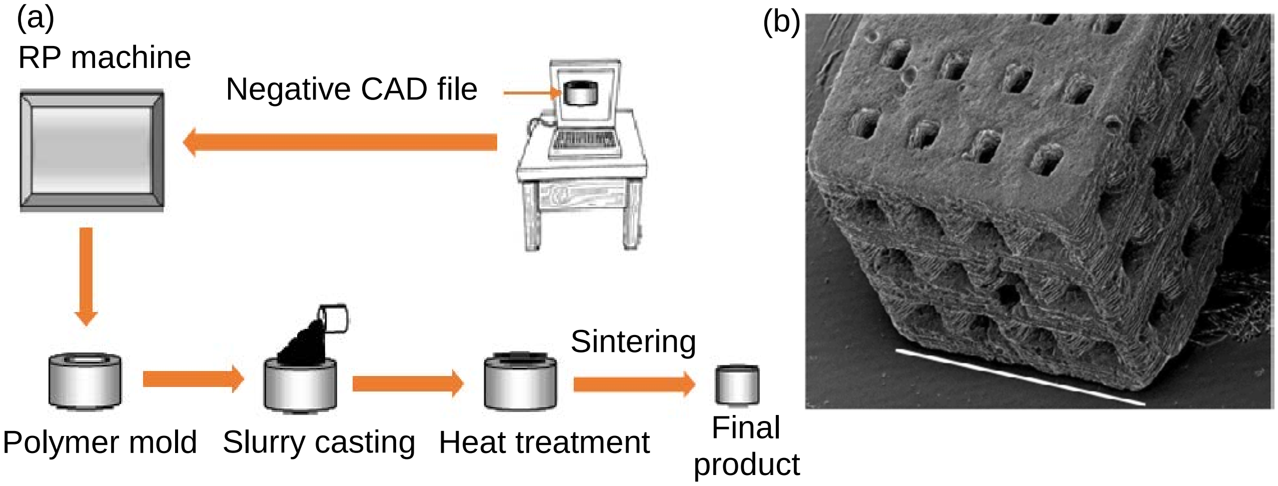

Figure 2.12 (a) Schematic representation of the steps involved in rapid prototyping for fabrication of porous ceramic parts [45] and (b) SEM micrograph of a typical scaffold processed by RP technique (length of the white bar is approximately 3.6 mm) [46].

deposition modeling (FDM) [42], solid ground curing (SGC), and ink jet printing [43, 44, 37]. In all the RP techniques, 3D architectures are built directly by layer by layer deposition of materials [44]. Fig. 2.12(a) shows a schematic representation of processing steps involved in rapid prototyping and Fig. 2.12(b) depicts an ESEM micrograph of sample produced by rapid prototyping, revealing smooth horizontal and textured vertical surfaces as well as semi-spherical surface pores. Porous ceramics with both the cellular and periodic structures can be fabricated with a relatively higher level of accuracy in comparison to the other fabrication techniques. Compared to all other techniques discussed for fabrication of porous ceramics, a distinct advantage of this is the ability to create highly complex porous architectures with well controlled pore morphology. However, the manufacturing cost associated with the RP techniques are considerably higher relative to the other techniques [2].

All the above techniques are utilized to fabricate cellular ceramics for various applications. Recently, another technique freeze casting (also called ice-templating) has received significant attention because of the ability to develop bio-inspired novel porous ceramics, which can be post-processed to dense hybrid materials. This technique exploits the anisotropic growth characteristics of solvent crystals and phase segregation of particulate suspensions under unidirectional freezing conditions to develop hierarchical porous solids. Although various solvents have been attempted, water remains as the predominantly employed freezing vehicle because of the availability and similarity of the resultant structure with the natural solids that are of major interests to design bio-inspired materials. A key feature of the freeze-cast porous solids is the presence of tunable anisotropic pore morphology with low tortuosity that is highly suitable for structural, biomedical, and energy storage applications. Moreover, within a wide range of porosity freeze-cast porous ceramics exhibit significantly greater compressive strength in comparison to isotropic porous ceramics processed using the other techniques. Over the past decade, a large number of investigations focused on understanding the fundamentals of the freeze casting technique and significant progress is made on the development of processing-microstructure relationships. In comparison, structure-property (both mechanical and functional) relationships are yet to be well established. To this end, this thesis develops a custom-made device for unidirectional freeze casting of particulate suspensions to enable the investigation of the microstructure evolution and uniaxial compressive response of ice-templated sintered Al_2O_3 scaffolds processed from two different particle sizes as a function of the suspension concentration and freezing front velocity (FFV). The following, is a journey into the fundamentals of the dynamic interactions of an advancing freezing front with the particles present in a suspension under unidirectional freezing conditions, which builds the foundation of the principles exploited in the freeze casting technique to fabricate anisotropic porous solids. However, the following discussion is limited to only the unidirectional freezing of aqueous suspensions.

2.3 UNIDIRECTIONAL FREEZING OF AQUEOUS PARTICULATE SUSPENSIONS

During freezing of aqueous particulate suspensions under the influence of an applied unidirectional temperature gradient, solidification results from a phase segregation process in which the solvent crystalizes and the particles are ejected by the growing solvent (ice for aqueous systems) crystals [47-57]. In general, the morphological transition of the aqueous suspension during the unidirectional solidification is strongly influenced by the ice growth velocity [48]. Figure 2.13

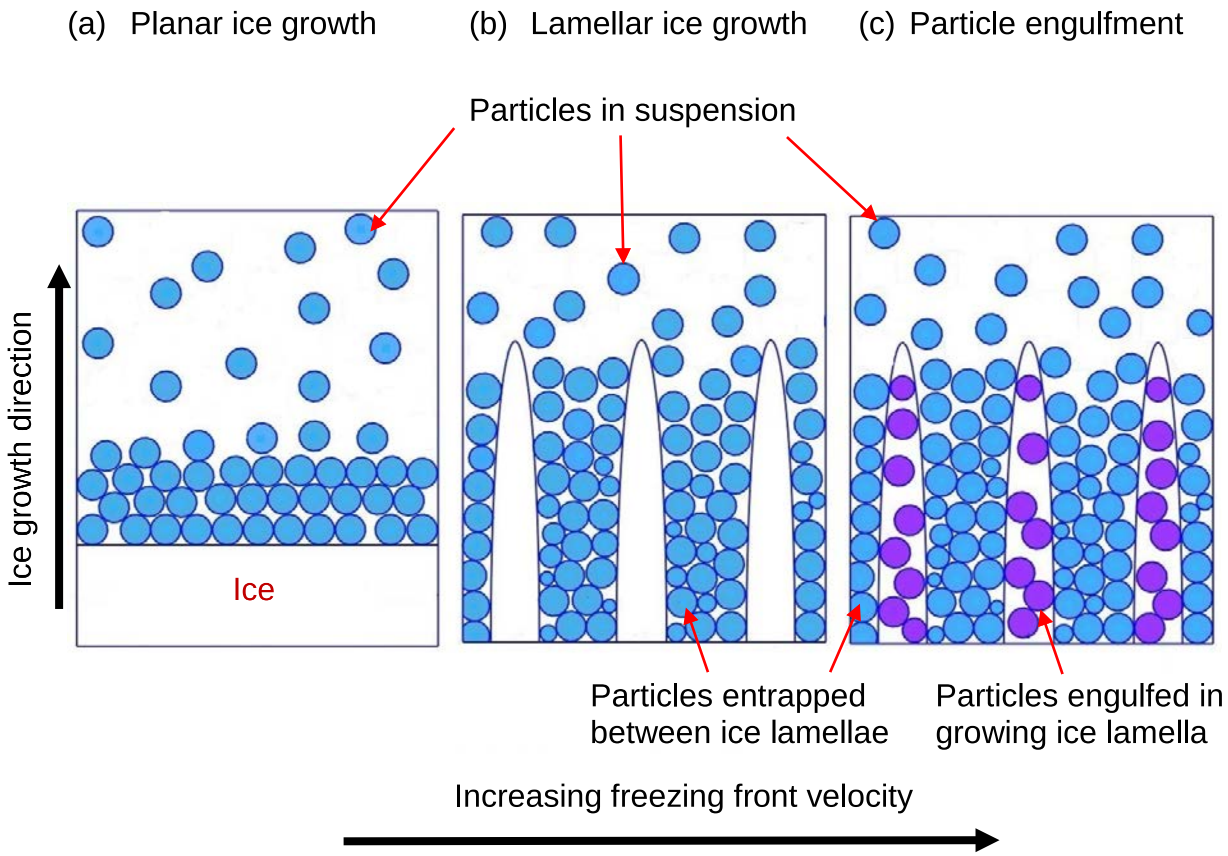

Figure 2.13: Morphological developments during unidirectional freezing of aqueous particulate suspensions depending on the freezing front velocity (FFV): (a) at very low FFV a planar ice front develops and the particles are pushed ahead of the advancing ice front, (b) at moderate FFVs splitting of the planar ice front leads to a lamellar morphology of alternating layers of ice crystals and consolidated particles, and (c) at high FFVs particles are engulfed within the ice crystals causing a loss of ordered structure [50].

depicts three different scenarios of the interaction of the growing crystals with the particles in the suspension under the unidirectional freezing conditions [49]. For a very slow ice growth (≤ 1 μm/s), a planar ice front develops that pushes the particles ahead (Fig. 2.13a) and as a result, a dense material structure is obtained. As the ice growth velocity increases, the interaction of the ice crystals with the particles becomes substantial. As a result, the planar ice front becomes non-planar (columnar) and the particles are ejected by the advancing ice front and accumulate in between the growing ice crystals (Fig. 2.13b). As this process continues, a lamellar morphology evolves within the unidirectionally solidified suspension that consists of the alternating layers of the ice and ceramic particles. With the further increase of the ice growth velocity particles start to get entrapped within the ice crystals due to rapid solidification and eventually beyond a critical FFV particles are completely entrapped (engulfed) within the ice crystals. This leads to a complete loss of the lamellar morphology and the frozen suspension attains a cellular morphology [50]. Therefore, to ensure the development of lamellar porous morphology, ice-templating of aqueous ceramic suspensions is typically conducted within the FFV range few μm/s to tens of μm/s. After the completion of freeze casting of aqueous particulate suspension, the solidified suspension is thereafter subjected to sublimation process such that the ice crystals can be removed without melting, which results a porous ceramic that is usually sintered at high temperature to partially densify and strengthen the porous structure. It is of note that solidification of the particulate suspensions is the most critical step in the freeze casting process, because the final pore morphology and pore size of the porous ceramics are primarily governed by this stage.

Formation of the lamellar morphology in the freeze-cast porous ceramics that are processed from aqueous suspensions is primarily attributed to the anisotropic growth characteristics of ice crystals [51]. Figures 2.14a and 2.14b show the crystal structure of ice and the growth characteristics of

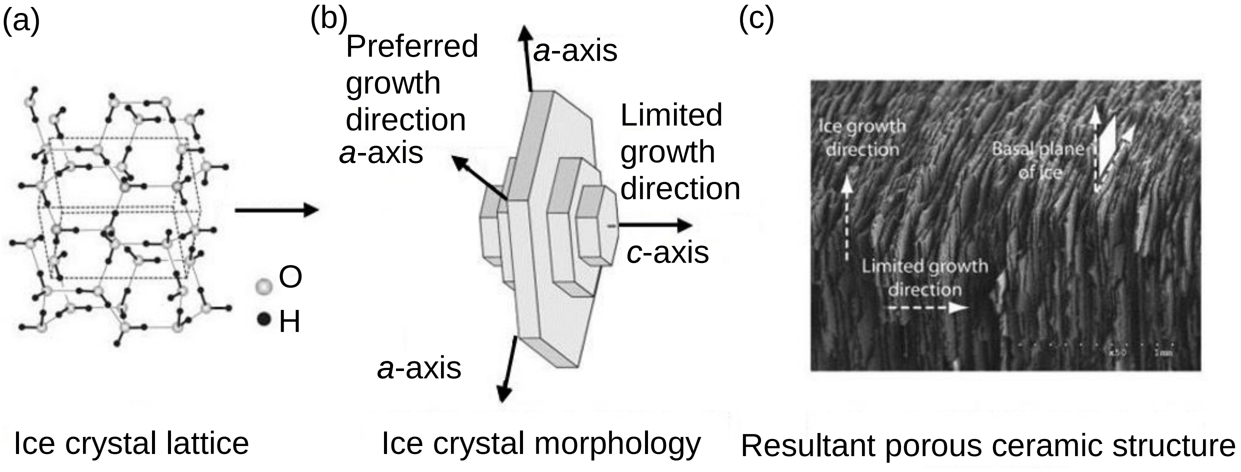

Figure 2.14: (a) Crystal structure of ice and (b) anisotropy of crystal growth kinetics, leading to lamellar ice crystals. The anisotropy of the growth kinetics is reflected in the final porous structures (c) obtained after sublimation and sintering. The direction perpendicular to the ceramic platelets corresponds to the limited growth direction of ice crystals [51].

the ice crystals, respectively, which relate to the lamellar morphology that evolves during the ice-templating [51]. Ice has a hexagonal crystal structure and due to the anisotropic crystal structure, ice growth characteristics are different along the crystallographic axes. As illustrated in Fig. 2.14b, ice front velocity parallel to the *c*-axis is about 10^2 to 10^3 times lower in comparison to that perpendicular to the *c*-direction. Therefore, during freezing once the ice crystals form, ice platelets with a very large anisotropy then develop due to very fast ice growth along the *a*-axes in comparison to *c*-axis. Under an applied unidirectional thermal gradient, the freezing process is easier for the crystals whose *c*-axes are perpendicular to the temperature gradient, resulting in the growth of the ice crystals along *a*-direction that is oriented along the applied temperature gradient. Therefore, ice crystals with horizontal *c*-axes will grow at the expense of the others and continue to grow upward, resulting in an architecture that is composed of long vertical lamellar crystals with horizontal *c*-axes. In the final structures, the direction perpendicular to the lamellae corresponds thus to the original *c*-axis of ice crystals (Fig. 2.14c) [51].

Figure 2.15 shows critical steps of freeze casting (ice-templating) [52]. First, appropriate quantities of ceramic powders, dispersant, organic binder, and water are mixed to prepare suspensions. A dispersant is used to stabilize a suspension and minimize settling of the powder particles. A binder provides strength to the ceramic bodies prior sintering to ensure safe handling of green bodies. Suspensions are then solidified under unidirectional freezing conditions. Typically, ceramic suspension is poured into a cylindrical mold and bottom surface of the mold is gradually cooled from room temperature to a temperature well below the freezing temperature of the solvent (0°C for water). For aqueous suspensions, as the bottom surface temperature goes below 0°C, ice

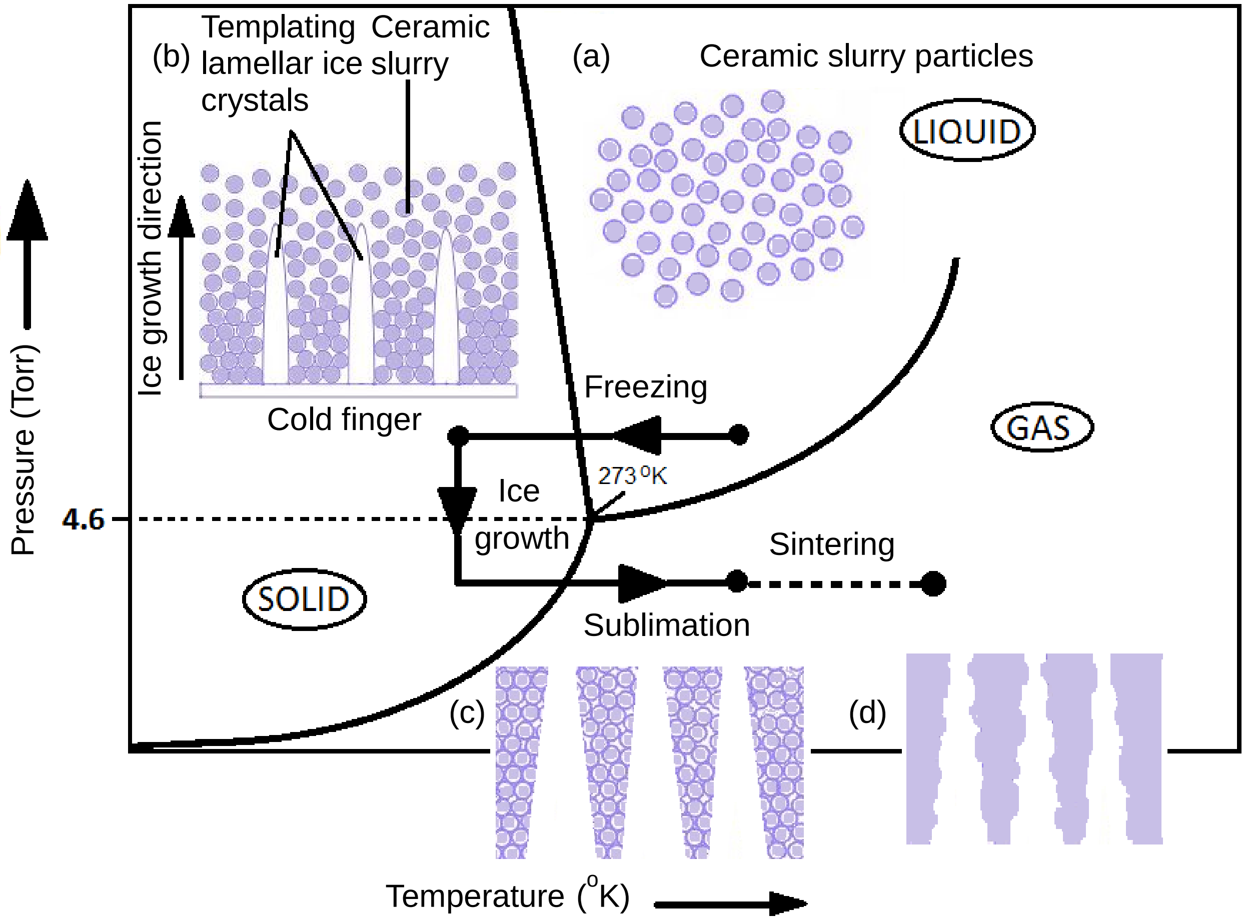

Figure 2.15: Processing steps of freeze casting (ice-templating): (a) aqueous ceramic suspension preparation, (b) unidirectional freezing, (c) sublimation, and (d) sintering. [51]

crystals nucleate at the contact points of the cold surface and suspension, and will grow in the direction of the applied temperature gradient (bottom to top of the mold). As the ice crystals start growing vertically, particles in the suspension are ejected from the advancing solidification front and concentrate in between the growing ice layers (Fig. 2.15b). As the process continues, a lamellar microstructure containing alternate layers of ice and ceramic particles develop that is oriented in the direction parallel to the movement of the freezing front. After completion of the solidification process, ice crystals are sublimated at low temperature and reduced pressure, which results in a porous structure containing ceramic layers and oriented pores (Fig. 2.15c). After sintering, ceramic layers densify and the overall porous structure gains strength, but the porosity and pore morphology created by the ice crystals during the ice-templating are retained (Fig. 2.15d).

CHAPTER 3

A CUSTOM-MADE UNIDIRECTIONAL FREEZE CASTING DEVICE

Freeze casting typically involves solidification of a particulate suspension under an influence of a unidirectional temperature gradient that facilitates anisotropic growth of solvent crystals. Therefore, freeze casting technique requires a device that can enable unidirectional freezing of particulate suspensions under well-controlled cooling conditions. Although the technique is simple in principle, there is no commercial set up available yet that can be readily employed to process materials under unidirectional freezing conditions. Therefore, one major goal of this thesis is to develop a custom-made device that allows to fabricate cellular ceramics under an applied unidirectional freezing conditions. It is to note that the setup is not only employed for the research undertakings of this thesis, but is also central to several other research activities in the Laboratory of Extreme and Energy Materials (LEEM) at Old Dominion University. Figure 3.1 shows schematics of few freeze casting devices that have been utilized by other research groups for unidirectional [2] and bidirectional freeze casting [58]. Use of the bidirectional freeze casting set

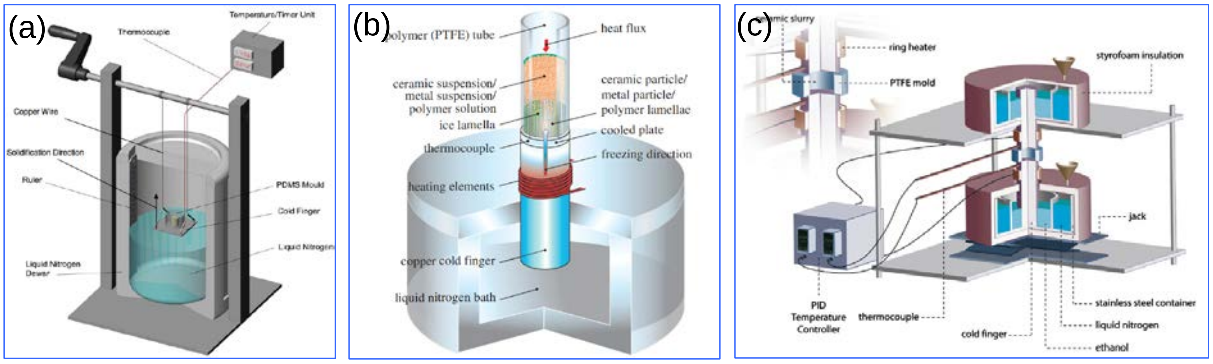

Figure 3.1: Schematics of freeze casting set up for (a-b) unidirectional [2] and (c) bidirectional freezing [58] of particulate suspensions.

up, however, is extremely limited and mainly used to obtain extremely fast freezing front velocity (>100 μm/s) [58]. Although these devices appear to be different, all of them employ the same unidirectional freezing principle discussed in Chapter 2. In the following, first the freeze casting set up developed in this thesis is presented and next all the processing steps employed to fabricate freeze-cast cellular ceramics are described.

3.1 EXPERIMENTAL SET UP FOR UNIDIRECTIONAL FREEZE CASTING

Figure 3.2 shows a schematic of the unidirectional freeze casting device designed and developed in this thesis. Although this custom-made device is similar to that shown in Fig. 3.1a, several modifications were made for better maneuver of the system. However, there was no intent to make any comparison with the setup shown in Fig. 3.1a. In the following, first a brief description of the setup is provided followed by a detail discussion of the step-by-step operating procedure employed during freeze casting. The main components of this custom-made device are a liquid Nitrogen (L-N_2) Dewar, a thin steel plate (cold finger, thickness ~0.5 mm), and a cryogenic temperature measurement system that records temperature changes in the cold finger during freeze casting. L-N_2 is employed as the freezing media to achieve temperature of suspensions as low as -100°C. Additionally, a mechanism was devised that allows the measurement of the L-N_2 level within the Dewar, and adjust the gap in between the L-N_2 top surface and the cold finger. A Teflon mold containing ceramic suspension is placed on the cold finger, and the assembly is inserted within the Dewar and placed at a specified height above the L-N_2 surface. Since the temperature of the cold finger and bottom of the suspension in contact with the cold finger reduces rapidly in comparison to the top of the suspension, the suspension within the mold is subjected to a unidirectional temperature gradient where the temperature increases from bottom to top. For an aqueous

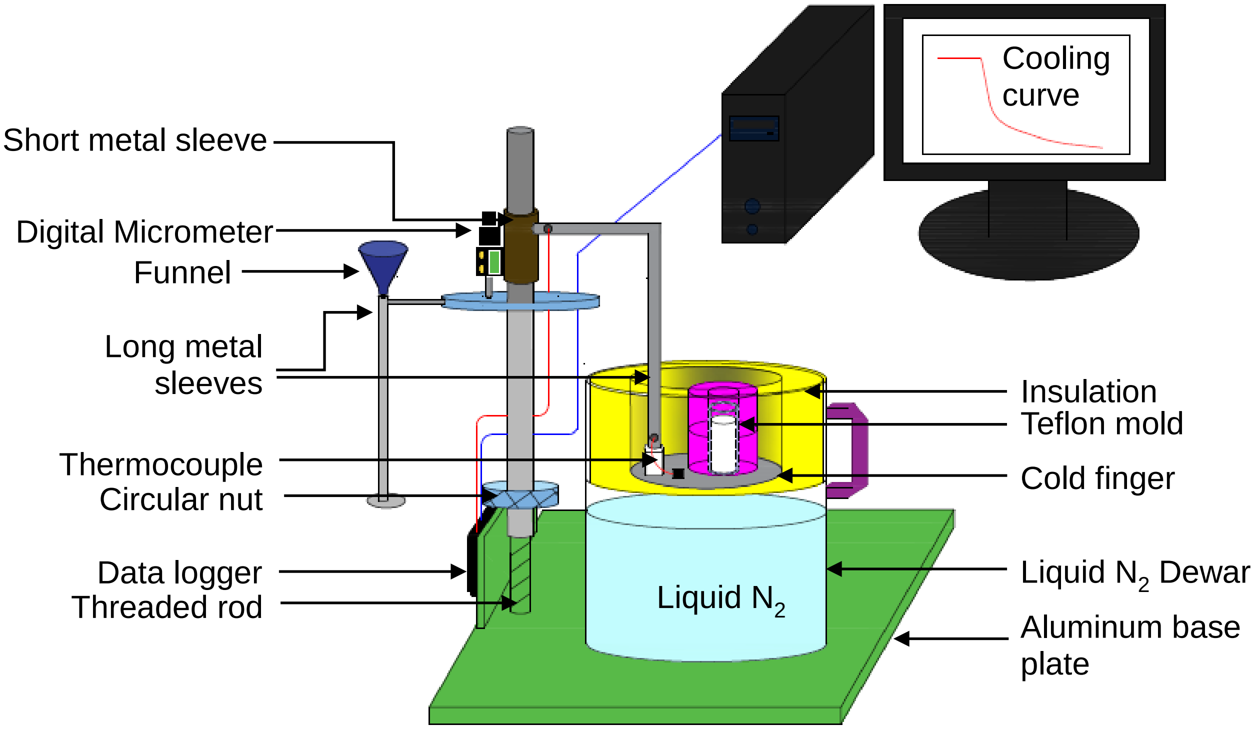

Figure 3.2: A schematic of unidirectional freeze cast set-up developed in this thesis.

particulate suspension, solidification starts as the temperature of the suspension reaches below the freezing temperature of water (0 °C) [51]. Ice crystals nucleate at the bottom of the suspension and grow upwards (vertically) under the influence of the applied unidirectional temperature gradient. The thickness of the cold finger, the L-N_2 quantity, and the gap in between the cold finger and the L-N_2 top surface (i.e., in between the L-N_2 top surface and bottom of the suspension) are the critical parameters that control the solidification kinetics of a particulate suspension during freeze casting. As discussed in Chapter 2, morphological evolution during unidirectional solidification and phase segregation of an aqueous ceramic suspension depends on the ice growth velocity, which is controlled by the unidirectional temperature gradient applied to the suspension. Therefore, control over the temperature changes of the cold finger is essential to achieve the desired range of ice growth velocities to ensure the formation of porous morphology during freeze casting. Once the solidification is complete, the frozen sample is removed from the mold and is ready for freeze-drying (discussed later). In the following paragraphs, a detailed description of the all the components of the device is provided.

The Dewar used in the experiment is a thermally insulated, cylindrical vacuum flask with a capacity of 3 L. This flask is designed to hold L-N_2 without minimum volume loss over a long period of time that is suitable for freeze casting experiments. As shown schematically in Fig. 3.2, the L-N_2 Dewar is placed on a thick aluminum base plate on which all the components of the device are attached. Leveling screws with rubber discs are attached to the base plate to ensure that the plate is parallel to the ground and avoid vibrations during an experiment. Adjustable stoppers are placed on the top surface of the base plate to fix the Dewar at the center of the plate. A metal plate is attached to one side of the base plate to mount the temperature measurement device and a threaded rod is attached vertically to the base plate to attach various components of the entire set up. A long metal sleeve concentric with the threaded rod rests on a circular nut, which is attached to the rod. As the nut rotates, the long metal sleeve can move vertically along the threaded rod. There are two L-shaped hollow arms that are attached to the set up. One end of one of the L-shaped arms (called L-N_2 level indicator) is fixed to a large metal disk, which is attached directly to the long metal sleeve towards the upper end, and a small metal plate is fixed at the other end of the arm. On the L-N_2 level indicator, a funnel is also attached at the top that is used for pouring L-N_2 into the Dewar. The other L-shaped arm holding the cold-finger at one end is attached to a short metal sleeve through the other end, where the short sleeve is concentric with the long metal sleeve. A digital micrometer is also connected to short metal sleeve, where the movement of the spindle of the micrometer controls the vertical movement of the short sleeve along the long sleeve. Both

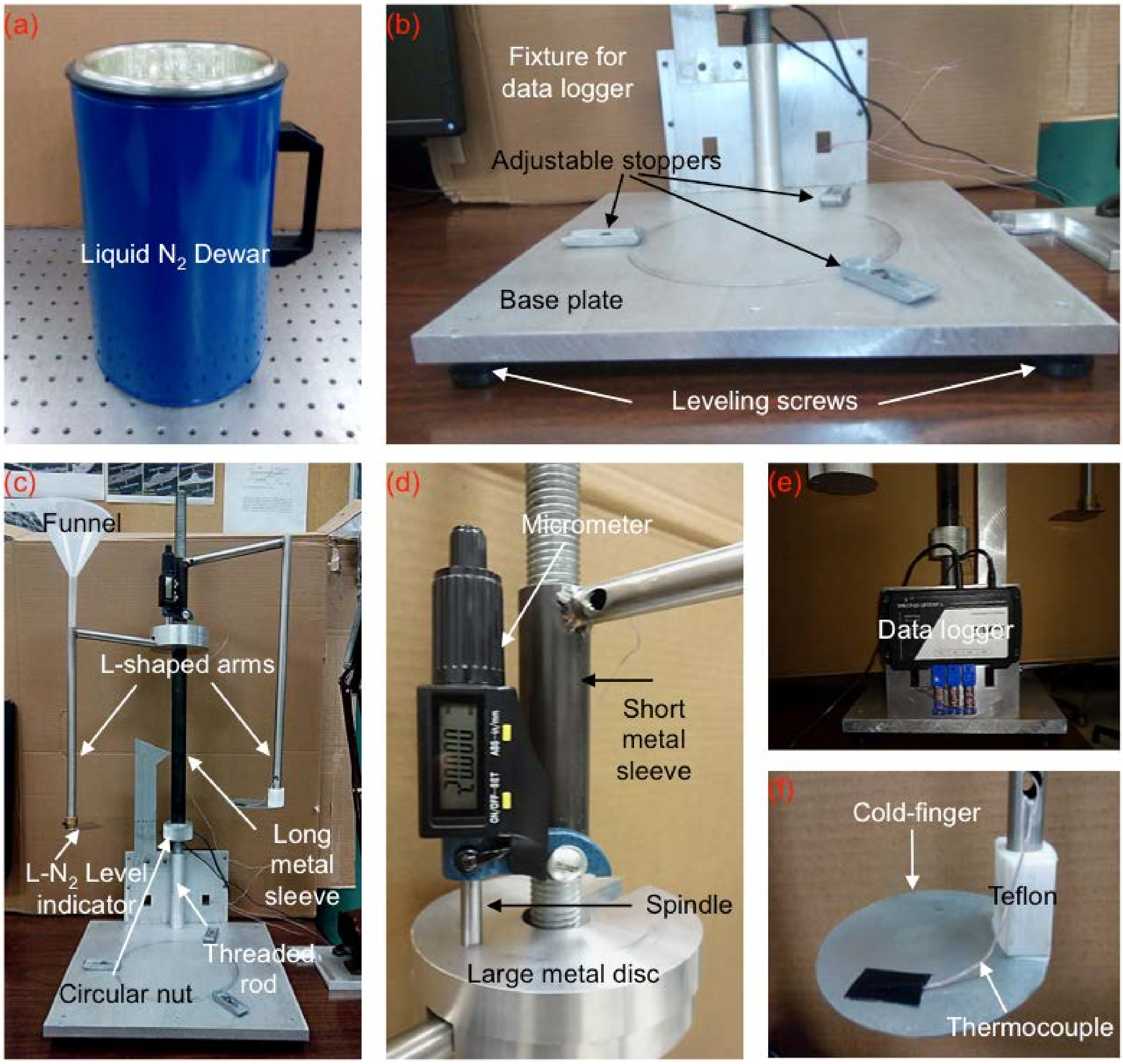

Figure 3.3: Images of the actual components of the custom-made freeze casting device: (a) liquid N_2 Dewar, (b) base plate, fixture for data logger, leveling screws, and adjustable stoppers, (c) L-shaped arms for the L-N_2 level indicator and cold finger, threaded rod and circular nut, (d) digital micrometer, short metal sleeve, and large metal disc, (e) data logger, (f) cold finger.

sides of the cold-finger (i.e., thin steel plate) are metallographically polished and circular shape (diameter ~90 mm) of the plate helps to maintain a uniform temperature distribution over the cold-finger. As illustrated in Fig. 3.2 the cold-finger is not directly attached to the L-shaped metal arm, rather is connected through a Teflon connector to minimize the heat transfer to the cold-finger from the metal arm. The angle in between the cold-finger and metal arm is 90°, which keeps the cold-finger parallel to the L-N_2 surface inside the Dewar. It is also of note that prior to start of an experiment, both the metal plate on the L-N_2 level indicator and cold-finger reside at the same height from the base plate. The low temperature measurement system consists of a 4-channel thermocouple data logger and a T-type thermocouple (Omega Engineering Inc., Stamford, CT), where the thermocouple is attached on the top surface of the cold finger. A T type thermocouple is chosen because it is suitable for extremely low temperature applications (e.g., cryogenics and ultra-low freezers) and has an excellent repeatability within the temperature range of -200°C to 350°C with an accuracy of +/- 1°C and sensitivity of about 43 µV/°C [information: Omega Engineering Inc.]. Actual images of all the components of the freeze casting set up described above are shown in Figure 3.3.

3.2 OPERATING PROCEDURE OF FREEZE CASTING SET UP

In this section, a step-by-step operating procedure of the freeze casting device is described, which is also schematically depicted in Fig. 3.4. As mentioned previously, amount of L-N_2 in the Dewar is one critical parameter to control the freezing kinetics. After conducting preliminary studies (not discussed here) and to ensure that both the cold finger and Teflon mold containing ceramic suspension are retained within the cooling zone inside the Dewar during freeze casting, it was decided to utilize 1.75 L of L-N_2 for each experiment. To begin a freeze casting experiment, the first step is thus to ensure that the desired volume of L-N_2 (1.75 L) is contained within the Dewar. For this purpose, the L-N_2 level indicator is inserted inside the Dewar (Fig. 3.4a), which can move vertically on the threaded rod to adjust the position for different volume of L-N_2 in the Dewar.

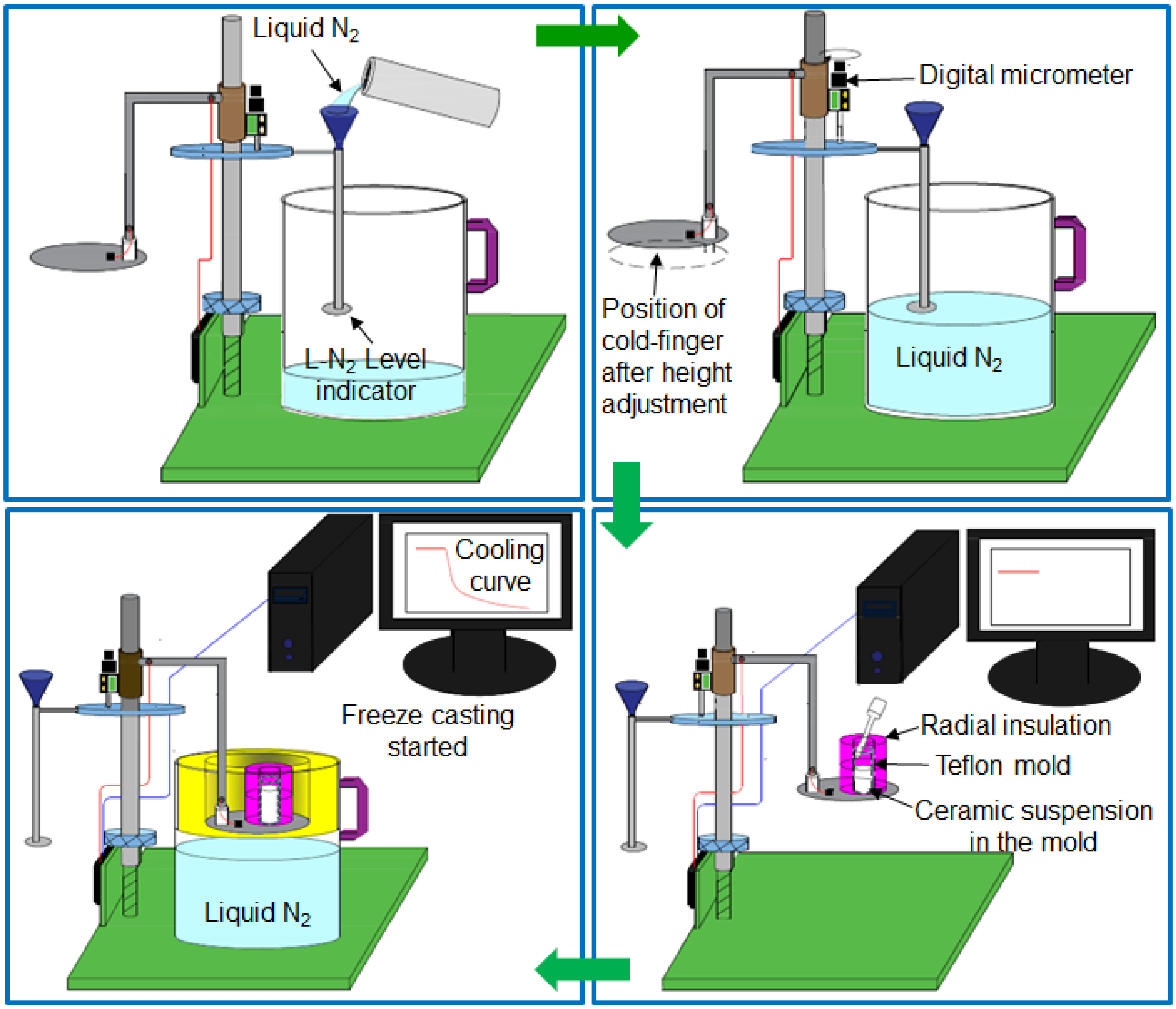

Figure 3.4: Schematic representation of the step-by-step operational procedure of the unidirectional freeze casting set up. (a) pouring of L-N_2 in to the Dewar, (b) adjustment of gap between L-N_2 and cold finger by digital micrometer, (c) transfer of ceramic slurry in to Teflon mold, (d) start of freeze casting experiment.

Afterwards, L-N_2 is poured into the Dewar through the funnel until top surface of the liquid touches the metal plate of the level indicator (Fig. 3.4b). This indicates that desired volume of L-N_2 (1.75 L) is present within the Dewar. The level indicator is then moved out of the Dewar. The next step is to adjust the gap in between the cold finger and top surface of L-N_2, which is performed using the digital micrometer. As the spindle moves out of the micrometer, the L-shaped arm containing the cold-finger moves upward and digital reading on the micrometer indicates the magnitude of the vertical displacement. Using the micrometer, the cold-finger is displaced upward until a desired gap in between the cold-finger and L-N_2 is achieved (Fig. 3.4b). As mentioned previously, by adjusting the gap in between the cold-finger and L-N_2, unidirectional temperature gradient and thus the freezing front velocity are controlled. In the next step (Fig. 3.4c), a Teflon tube (ID 19 mm, wall thickness 3.2 mm, height 72 mm) is placed on the cold-finger, which is utilized as a mold to contain ceramic suspension during the freeze casting. Both the ends of the Teflon tube are polished to make them flat and parallel. For each experiment, a small amount of grease is applied on the bottom surface of the mold to glue the mold on the cold-finger. This is done to ensure that there is no leakage of suspension from the bottom of the mold. However, care is taken to avoid any spread of the grease on the cold-finger inside the mold so that there is no grease in between the plate and suspension. Care is also taken while transferring the suspension to the mold so that no air bubbles get trapped within the suspension, which can cause defects in the processed materials. At this stage, the Teflon mold is radially insulated using a high-density polymeric foam to avoid any thermal gradient from the sides so that the suspension within the mold is subjected to only unidirectional temperature gradient during freeze casting experiment (Fig. 3.4c). Similarly, the upper part of the inner wall of the Dewar is also insulated to minimize radial thermal gradient to the mold (Fig. 3.4d). Once the mold is filled with the desired volume of ceramic suspension, the entire assembly is inserted inside the Dewar and temperature of the cold-finger decreases rapidly from room temperature (Fig. 34.d). This step initiates the unidirectional freezing of the ceramic suspension. The length of the freezing process varies within a range of 30-70 min depending on the ice growth velocity. Higher the gap in between the cold-finger and L-N_2, the lower is the freezing front velocity and longer will be freezing time. Having provided the operating procedure of the freeze casting device, the following sections briefly discuss the adjustment and estimation of freezing front velocities, ceramic suspension preparation, and freeze drying and sintering of freeze-cast samples.

3.3 CONTROL AND ESTIMATION OF FREEZING FRONT VELOCITIES (FFVS)

During unidirectional freeze casting of an aqueous ceramic suspension, ice crystals nucleate and grow from the bottom to the top of the suspension, i.e., in the direction of the applied temperature gradient. Ice-templated scaffolds transition from a dense layer to an isotropic cellular structure to eventually a lamellar morphology oriented in the direction of the applied thermal gradient that prevails for rest of the length of a sample [50, 58, 60]. This is because ice crystals initially grow very rapidly but a steady-state growth velocity is eventually reached. However, it is difficult to maintain a constant ice growth velocity or freezing front velocity (FFV) over long distances (cm) and a structural gradient is thus common to observe within the lamellar region [50, 51, 58, 60]. In this thesis, an average FFV was estimated for each freeze casting experiment using the time-temperature data obtained from the T-type thermocouple attached on the cold-finger. During a freeze casting experiment, initially the cold-finger is at room temperature but the temperature decreases rapidly as the cold-finger is placed close to L-N_2. It is assumed that ice nucleation at the bottom of the suspension occurs as soon as the temperature of the cold-finger reaches 0 °C and the corresponding time is considered as the start time of the freezing process. The top of the suspension is visually inspected frequently during the experiment for completion of solidification and the time when the top is solidified is considered as the end time of the freezing process. Average FFV is estimated by dividing the frozen sample height (measured after removal of the sample from the mold) with the time required to complete the solidification (i.e., the time difference in between the end time and start time of the freezing process).

Microstructure of an ice-templated cellular ceramic is influenced significantly by the FFV, which depends on the rate of cooling of the cold-finger. As mentioned previously, in the freeze casting set up developed here, rate of cooling of the cold-finger and thus FFV were controlled by adjusting the gap in between the cold-finger and top surface of L-N_2. Figure 3.5a shows the time-temperature plots measured from the cold-finger during freeze casting for four different gaps. It can be observed that for each gap, cold-finger first reaches a low temperature (about -20 °C) linearly within few minutes, which is followed by a decrease of the slope and for the rest of the duration of the experiment the plate temperature decreases approximately linearly. The maximum lowest temperature of the cold-finger reached during an experiment increases with the decreasing gap.

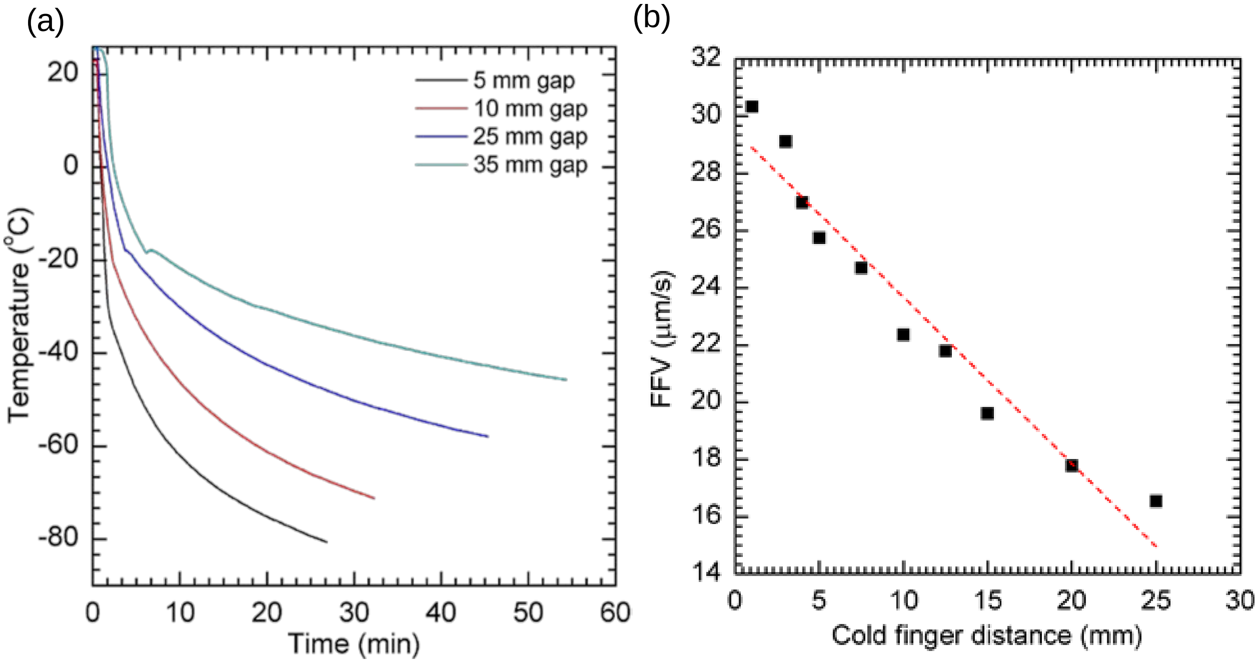

Figure 3.5: (a) Change of temperature of the cold-finger with time for four different gaps in between the cold-finger and top surface of L-N_2 and (b) cold-finger gap vs. average FFV.

Also, the greater the gap in between the cold-finger and L-N_2 the longer is the time required for completion of the freeze casting. Figure 3.5b shows the plot of cold-finger to L-N_2 surface gap vs. average FFV revealing an almost linear variation of the FFV with the gap. Within a gap of 3-25 mm, average FFV values in the range of 15-30 μm/s were obtained.

As discussed above, it is assumed that ice nucleation and growth started at the bottom of the ceramic suspension as soon as the temperature on the top surface of cold-finger reaches 0 °C. However, ice nucleation and growth may consume a finite amount of time and as a result, the estimated FFV values might present an underestimate of the actual average FFV. Therefore, an alternate procedure was also employed here for the estimation of average FFV. For this purpose, two fine holes were drilled on the mold wall from outside (to insert a thermocouple at each hole) at 3 mm and 42 mm heights from the cold-finger. However, a fine layer of Teflon is maintained in

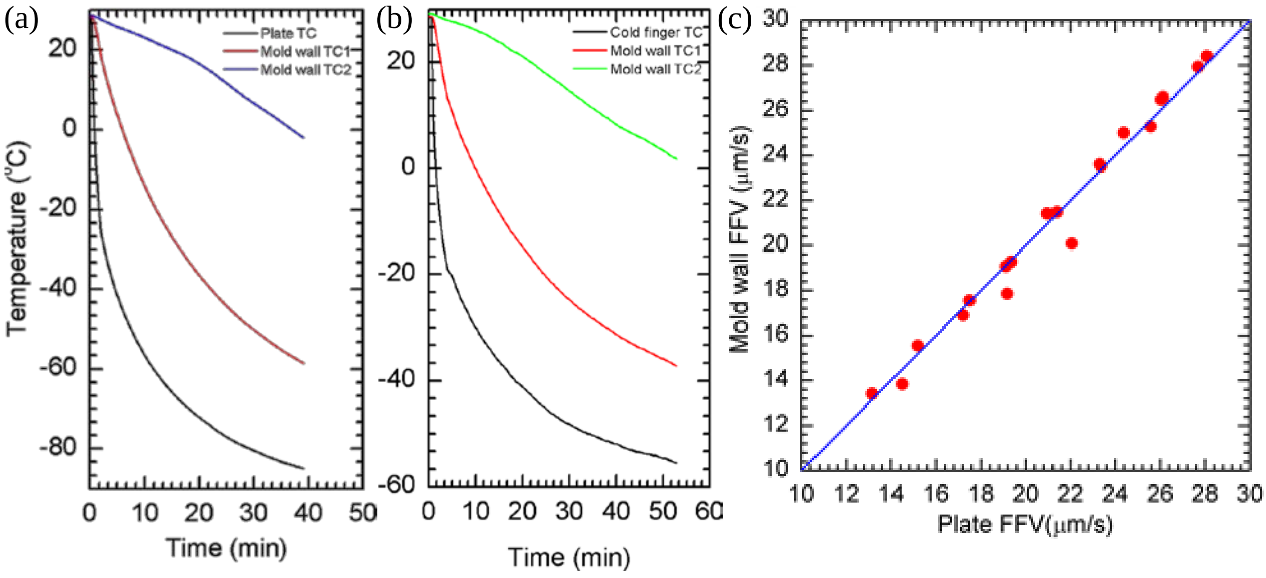

Figure 3.6: Variations of the cold-finger temperature and mold wall temperature with time at two different heights from the cold-finger (3 mm and 40 mm) for a cold-finger to L-N_2 gap of (a) 5 mm and (b) 25 mm. (c) average FFVs measured from thermocouple attached on cold finger vs. thermocouple attached on mold wall.

between the thermocouple and ceramic suspension so that the thermocouple does not come in contact with the suspension directly during freeze casting. Several experiments were conducted where time-temperature data were simultaneously collected from the cold-finger as well as from two different locations (3 mm and 40 mm) on the mold wall. The mold was filled with ceramic suspension up to a height of 45 mm from the cold-finger. Figures 3.6a and 3.6b show the measured time-temperature data corresponding to cold-finger (Plate TC) and mold wall (Mold wall TC1 for 3 mm and Mold wall TC2 for 40 mm) for gaps of 5 mm and 25 mm, respectively. During an experiment, a thermocouple inserted into the mold wall will record 0 °C as the ice front passes through the height where the thermocouple is located [61]. Therefore, both the thermocouples inserted into the mod wall at 3 mm and 40 mm heights will record 0 °C but at different times. From this time difference and using the height difference (37 mm), average FFV was also estimated. Figure 3.6c shows a plot of the average FFV values estimated from the cold-finger vs. average FFV values estimated from thermocouples on the mold wall for various cold-finger gaps. It can be seen that the ratio of the average FFVs estimated from two different methods is almost 1, suggesting that both are equally applicable for the estimation of the average FFVs. Based on this observation, it was decided to utilize the time-temperature data measured from the cold-finger for the estimation of average FFV.

3.4 PROCESSING OF CELLULAR CERAMICS USING THE CUSTOM-MADE FREEZE CASTING DEVICE

In this section, all the processing steps that are involved in freeze casting are briefly discussed. Towards the end of this section, few representative scanning electron microscope (SEM) images of the sintered porous alumina (Al_2O_3) ceramics are presented to demonstrate the control over the

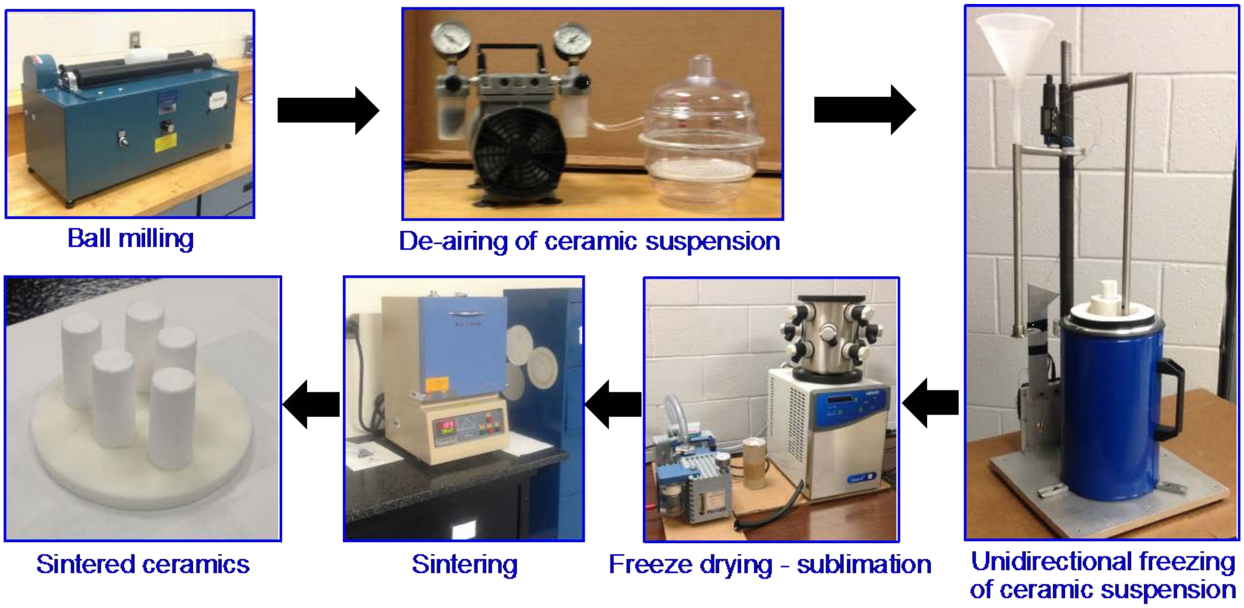

Figure 3.7: Processing steps involved in fabrication of porous ceramics using unidirectional freeze casting.

freeze-cast microstructure development. Figure 3.7 shows all the processing steps employed in this thesis for processing of porous ceramics using freeze casting. Since the time requirement of unidirectional solidification of a ceramic suspension in freeze casting process typically ranges from 30-60 min, preparation of a well-dispersed aqueous suspension is important. For this purpose, aqueous ceramic suspensions were prepared using a ball mill. First the required amount of ceramic powder, deionized water and milling media (zirconia, ZrO2, spheres of 5 mm diameter) were mixed in a Nalgene bottle. To stabilize the suspension, small amount of a dispersant (typically 0.5 wt.% of the powder) was also added to the suspension. Next, the suspension was ball milled for 24 hours. After completion of ball milling, a binder was added to the suspension (typically 5 wt.% of the powder) and mixed for another hour. Afterwards, the ZrO_2 spheres were separated from the suspension followed by de-airing for 30 min.

Next, the custom-made device developed here was employed for the unidirectional freeze casting. In the current work, gap in between the liquid N_2 and cold-finger was varied systematically to achieve average FFV values in the range of 12-34 μm/s. After completion of the freeze casting, the frozen sample was removed from the mold and stored in a refrigerator temporarily. All the freeze-cast frozen samples were approximately 19 mm in diameter and 45 mm in height. Afterwards, the frozen samples were freeze-dried (Freeze Dryer 2.5L, Labconco, Kansas City, MI) for 96 hours at a low pressure (0.014 mbar) and temperature (-50°C). Next, the freeze-dried samples were sintered in a box furnace (KSL-1700X, MTI Corporation, Richmond, CA) using the following time-temperature schedule: (i) heated from the room temperature to 450°C at a rate of 3°C/min and held for 4 hours for the binder burnout, (ii) heated from 450°C to 1550°C at a rate of

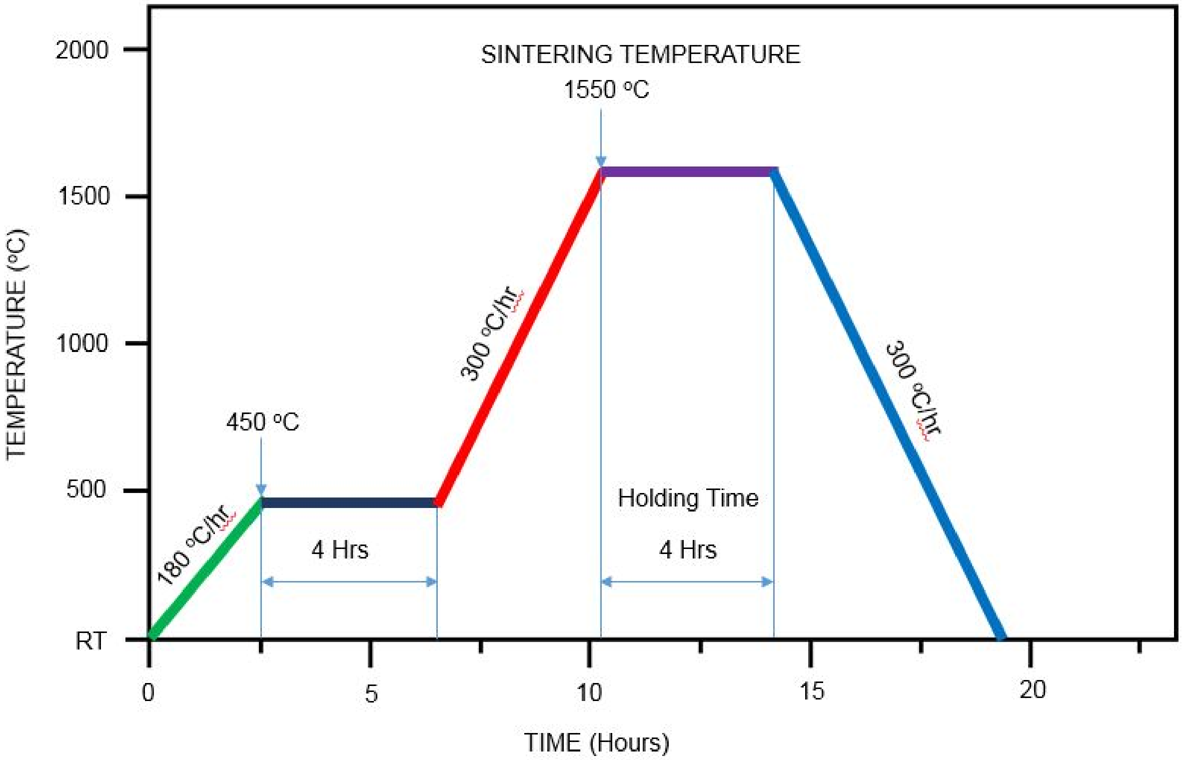

Figure 3.8: Schematic diagram of sintering regime for all green samples.

5°C/min and sintered for 4 hours, and (iii) finally cooled from the sintering temperature to the room temperature at a rate of 5°C/min (Fig. 3.8).

A desktop SEM was employed to investigate the microstructures of the sintered materials. Figure 3.9 shows a representative SEM micrograph (ice growth direction out of the page) of a sintered porous alumina (Al_2O_3) ceramic, which reveals relatively long-range order of ceramic lamellae walls and oriented pores. It can also be observed that there exist several lamellar regions that are randomly oriented with respect to each other as indicated by the thick yellow arrows. However, within each individual lamellar region ceramic walls are observed to be highly parallel. During unidirectional freeze casting of aqueous ceramic suspension, ice crystals nucleate randomly at the bottom of a suspension over the cold surface. While the unidirectional thermal gradient aligns the growing ice crystals in the direction of the alignment, there is, however, limited alignment that occurs along the radial direction. As a result, several randomly oriented colonies of ice crystals emerge that grow vertically under the influence of the applied temperature gradient and within

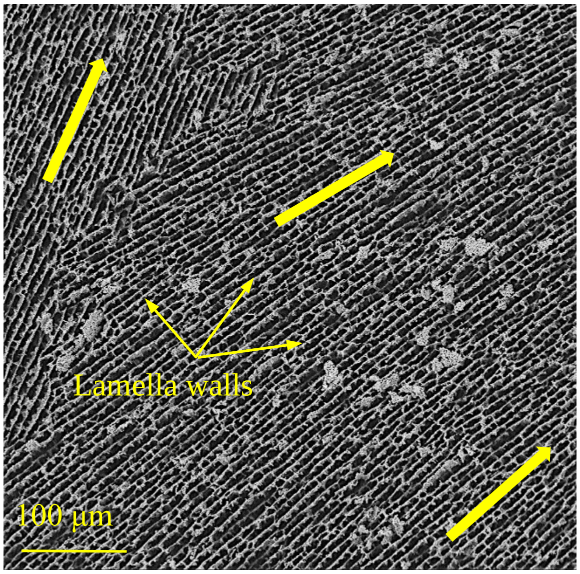

Figure 3.9: SEM micrograph revealing multilayered porous structure of sintered Al_2O_3.

each colony basal planes of the ice crystals remain mutually parallel. Sublimation of the phase segregated and solidified suspension results in lamellar pore morphology with random oriented lamellar domains, as observed in Fig. 3.9. Figures 3.10a and 3.10b show the SEM micrographs revealing microstructures of freeze-cast sintered porous Al_2O_3 ceramics, which were processed at relatively high (29.4 µm/s) and relatively low (15.5 µm/s) FFVs (ice growth direction out of the page). While both the SEM micrographs show lamellar pore morphology, both the thickness of the lamellae walls and interlamellae spacing are observed to decrease with the increasing FFV. This occurs because with increasing FFV more number of ice crystals nucleate and as a result finer freeze-cast microstructure is obtained. These observations are consistent with the results reported by others. Overall, the microstructural investigations support that the custom-made device successfully developed porous ceramics with well-controlled microstructures.

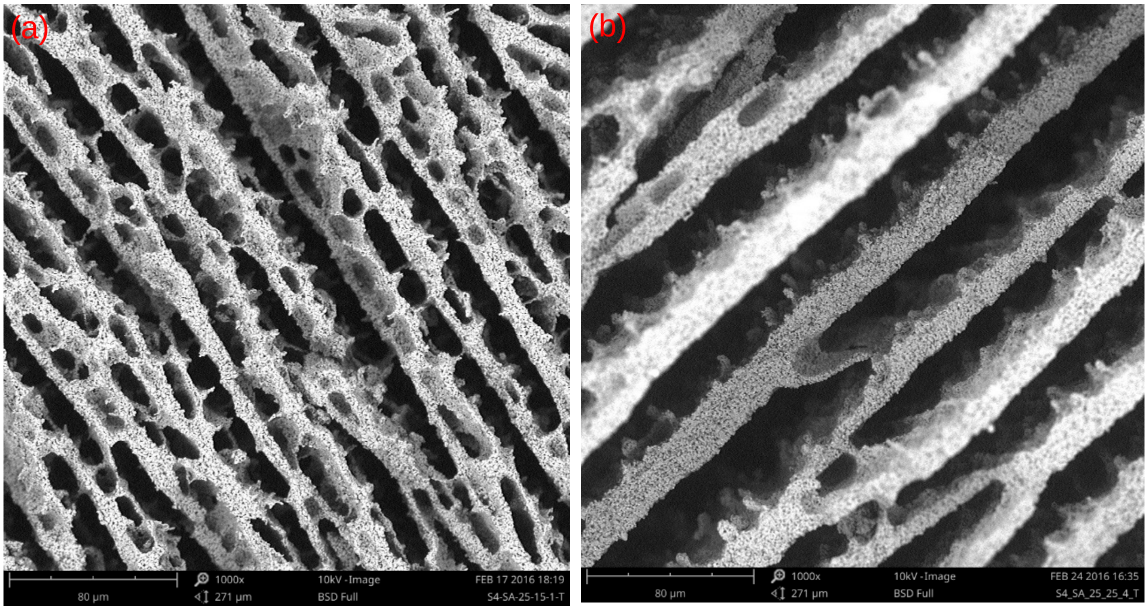

Figure 3.10: SEM micrographs revealing microstructures of freeze-cast sintered porous Al_2O_3 ceramics, processed at (a) a relatively high (29.4 µm/s) and (b) a relatively low (15.5 µm/s) FFVs (ice growth direction out of the page).

CHAPTER 4

A COMPARISON OF MICROSTRUCTURE AND UNIAXIAL COMPRESSIVE RESPONSE OF ICE-TEMPLATED ALUMINA SCAFFOLDS FABRICATED FROM TWO DIFFERENT PARTICLE SIZES

Freeze casting (ice-templating) is an emerging processing technique to develop anisotropic ceramic scaffolds that are promising for bone-tissue engineering, solid-state battery electrodes, solid oxide fuel cells, impact energy-absorption, and other structural applications [47, 52, 58, 61-68]. In this technique, an aqueous or non-aqueous particulate suspension is solidified under a unidirectional temperature gradient and subsequent sublimation of the frozen solid results in an anisotropic porous microstructure that is a replica of the frozen solvent structure. Afterwards, green bodies are sintered to partially densify and strengthen the scaffolds but without altering the overall pore architecture. Although various solvents are employed as a freezing vehicle, water results in a tunable lamellar pore morphology that can meet the demand of anisotropic scaffolds with low pore tortuosity. Most of the available studies on freeze casting are focused on understanding the inherent process-microstructure correlations and, therefore, the understanding of the structure-property (mechanical in particular) relationships has been limited. While the total porosity depends mainly on the solids loading of a suspension, [47, 52, 58, 61, 65, 69] freezing conditions can be varied to tune the microstructural entities such as the lamella thickness and interlamellae spacing, interlamella bridge density, pore size, aspect ratio and morphology, and lamella walls roughness; all of which can have profound influence on the mechanical performance of the ice-templated scaffolds [47, 52, 58, 61-65, 70-73]. Microstructure evolution of the freeze-cast scaffolds as a function of the solids loading, freezing rate, suspension viscosity, pH and type of soluble additives, and their relation to compressive mechanical response has been addressed to some extent [52, 58, 61, 63-65, 70-73]. However, very little attention is given to the effects of the variation of the particle size on the microstructure and mechanical response of ice-templated sintered scaffolds.

During unidirectional solidification of an aqueous particulate suspension, ice crystals nucleate and grow from the bottom to the top of the suspension, i.e., in the direction of the applied temperature gradient. Solid particles can either be trapped within the growing ice crystals or be rejected by the ice front and concentrate in between the ice lamellae. There exists a critical freezing front velocity above that particles will remain engulfed within the ice crystals and the critical velocity increases with a decreasing particle size [50, 52, 74]. Therefore, at a comparable freezing front velocity (FFV) smaller particles will have a greater tendency to be ejected by the advancing ice front in comparison to the relatively larger particles. As a result, smaller particles tend to promote the

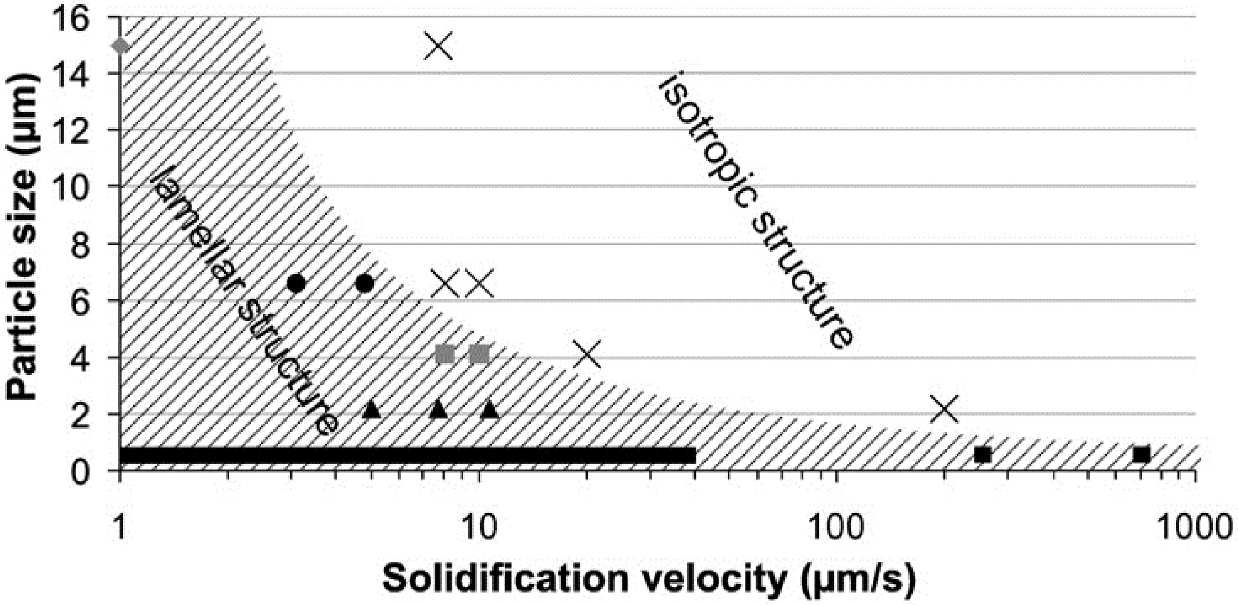

Figure 4.1: Influence of particle size on the microstructure development as function of solidification velocity [50].

formation of a relatively more lamellar morphology relative to the larger particles. Waschkies et al. [50] experimentally developed a processing-pore morphology (lamellar vs. isotropic) map as a function of the particle size (Fig. 4.1), which shows that at a given FFV unsintered freeze-cast alumina (Al_2O_3) scaffolds can transition from a fully lamellar to a completely isotropic cellular morphology with the increasing particle size. In other words, their study suggests that the FFV corresponding to lamellar to isotropic pore morphology transition continues to shift to lower values with a gradual increase of the particle size.

While the experimentally derived processing maps provide valuable insights into the particle size-pore morphology relationships, very little can be understood on the particle size dependence of the mechanical response of the ice-templated sintered scaffolds. As the pore morphology of the scaffolds transitions from the lamellar to dendritic to isotropic structure with the increasing particle size, an increase of the interlamella bridge density and thus decrease of the pore size is expected to enhance the compressive strength. [61, 65] Therefore, for a given ceramic suspension composition and FFV, strength of the scaffolds can be expected to increase with the increasing particle size. On the other hand, particle size is known to influence the particle packing in between the ice lamellae where the packing efficiency can deteriorate with the increasing particle size [75]. This may lead to the generation of the microporosity within the lamellae walls, which can be detrimental to the strength of the scaffolds. Furthermore, sinterability of ceramic powders decreases with the increasing particle size [76]. Therefore, the total porosity of the ice-templated scaffolds may increase due to increase of the ceramic walls porosity with the increasing particle size, which, in turn, can deteriorate the strength of the scaffolds. To that end, this work fabricated ice-templated scaffolds from Al_2O_3 powders of two different particle sizes (0.3 µm and 0.9 µm) as a function of the solids loading and FFV, and investigated the effects of the particle size variation on the microstructure of the sintered scaffolds and their uniaxial compressive response. Here, Al_2O_3 is chosen as a model material system but the results are equally applicable to other particulate systems also.

4.1 EXPERIMENTAL

4.1.1 Ceramic suspension preparation

Ice-templated scaffolds were processed from the commercially available α-Al_2O_3 powders of two different particle sizes: (i) d_{50} - 0.3 µm (surface area 8 m^2/g, APA-0.5, Sasol, Tuscan, AZ) and (ii) average particle size ~0.9 µm (surface area 2-4 m^2/g, Alfa Aesar, Ward Hill, MA). Here, these two powders are referred to as the SA (submicron-Al_2O_3 powder for 0.9 µm particle size) and NA (nano-Al_2O_3 powder for 0.3 µm particle size). For each ceramic suspension, required amount of the Al_2O_3 powder and small amount (0.5 wt.% of the powder) of ammonium polymethacrylate anionic dispersant (Darvan C, R.T. Vanderbilt Co., Norwalk, CT) were mixed with deionized water, followed by ball milling for 24 hours using zirconia (ZrO_2) spheres of 5 mm diameter. Next, an organic binder poly (2-ethyl-2-oxazoline) was added to the suspension (5 wt.% of the powder) and mixed for another hour. Afterwards, the ZrO_2 spheres were separated from the suspension followed by de-airing for 30 min. For each type of powder, ceramic suspensions were prepared for three different solids loadings: 15, 25, and 35 vol.%.

4.1.2 Freeze casting and sintering

A custom-made device was employed for the unidirectional freeze casting of the Al_2O_3 suspensions. In this set up, a cylindrical Teflon tube is placed on the top of a thin (0.5 mm thickness) steel plate and filled with Al_2O_3 suspension. The whole assembly is next inserted within a liquid nitrogen (L-N_2) Dewar, and the ice crystals start to grow at the bottom of the suspension and propagate upwards under an influence of the applied temperature gradient. The mold (Teflon tube) is radially insulated to avoid horizontal thermal gradient and ensure that the aqueous suspensions were frozen only under the vertical (i.e., unidirectional) thermal gradient. By adjusting the gap in between, the steel plate and the liquid N_2 top surface, unidirectional temperature gradient and thus the FFV are controlled. A thermocouple attached on the top of the steel plate measures the temperature change during the freezing process. In the current work, the gap in between the liquid N_2 and steel plate was varied systematically to achieve average FFV values in the range of 12-34 $\mu m/s$ where an average FFV was estimated by dividing the frozen sample height with the time required to complete the solidification [69]. After freeze casting, the frozen sample was removed from the mold and stored in a refrigerator temporarily. All the freeze-cast frozen samples were approximately 19 mm in diameter and 45 mm in height. Afterwards, the frozen samples were freeze-dried (Freeze Dryer 2.5L, Labconco, Kansas City, MI) for 96 hours at a low pressure (0.014 mbar) and temperature (-50°C). Next, the freeze-dried samples were sintered in a box furnace (KSL-1700X, MTI Corporation, Richmond, CA) using the following time-temperature schedule: (i) heated from the room temperature to 450°C at a rate of 3°C/min and held for 4 hours for the binder burnout, (ii) heated from 450°C to 1550°C at a rate of 5°C/min and sintered for 4 hours, and (iii) finally cooled from the sintering temperature to the room temperature at a rate of 5°C/min. Sintered scaffolds processed from the suspensions with 15, 25 and 35 vol.% solids loadings will be referred to here as SA-15, SA-25 and SA-35 for the SA powder and NA-15, NA-25 and NA-35 for the NA powder.

4.1.3 Microstructure characterization, density measurements, and uniaxial compression testing

Ice-templated scaffolds fabricated under unidirectional freezing conditions transition from a dense layer to an isotropic cellular structure to eventually a lamellar morphology oriented in the direction of the applied thermal gradient that prevails for rest of the length of a sample [58, 65, 50]. Also, a structural gradient is common to observe within the lamellar region. In the current work, the microstructure of each Al_2O_3 scaffold was characterized from two different planes transverse to the freezing direction, [65] located at 5 mm (referred to as bottom plane) and 30 mm (referred to as top plane) heights, respectively, from the bottom of each sample (Fig. 4.2a). For each transverse plane, the followings were quantified: (i) lamella thickness (t) and interlamellae spacing/wavelength (μ), (ii) pore size, both the major axis (a) and minor axis (b), (iii) pore aspect ratio ($\chi_p = a/b$), and (iv) lamellae bridge density (ρ_b, described later). For each microstructural feature, at least 100 measurements were performed. Uniaxial compression experiments were

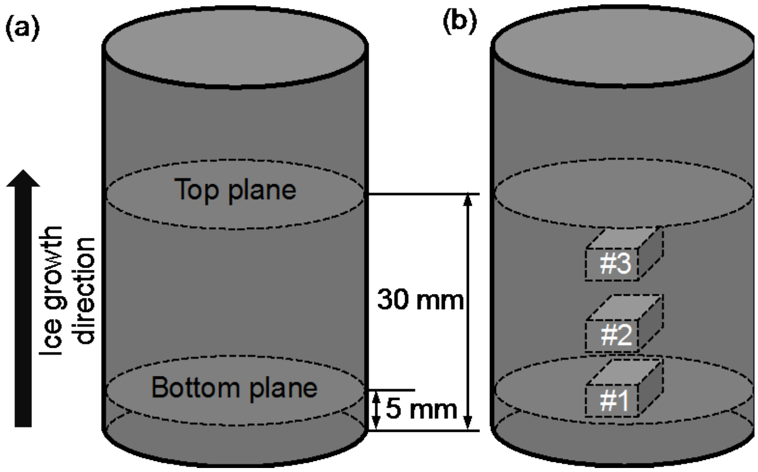

Figure 4.2: Schematic presentation of the locations of the (a) top and bottom planes, and (b) #1, #2 and #3 compression tests specimens.

conducted using a Tinius Olsen (model 10ST) mechanical testing machine equipped with a 5 kN load cell at a displacement rate of 0.5 mm/min. As shown in Fig. 4.2b, for each sintered Al_2O_3 scaffold, three specimens (referred to as #1, #2 and #3) were extracted from three different heights along ice growth direction for the compression tests. The density of each sintered specimen (ρ^*) was determined from the mass and dimension measurements, and the relative density (ρ_r) was estimated from ρ^*/ρ_s where ρ_s is the bulk density of dense Al_2O_3 ceramic (3.96 g/cm^3). Uniaxial compressive measurements were conducted along the ice growth direction on the specimens of dimensions 8 mm × 8 mm × 4 mm; 8 mm × 8 mm being the loading surface.

4.2 RESULTS AND DISCUSSION

4.2.1 Microstructure, relative density, and porosity

Figure 4.3 shows SEM micrographs of both the top and bottom planes of the sintered SA-15, SA-25, SA-35, NA-15, NA-25, and NA-35 scaffolds. For each composition, representative microstructures are shown for the scaffolds processed at the relatively low (13-18 μm/s) and relatively high (24-32 μm/s) FFVs. Irrespective of the powder particle size and suspension concentration, pore morphology of the sintered scaffolds at the relatively low FFV regime (Figs. 4.3a-f) is observed to be essentially lamellar with limited interlamellae bridging. However, for each composition a structural gradient is evident where the average lamella thickness, *t*, (i.e., ceramic walls thickness) and wavelength, μ, (both indicated in Fig. 4.3) increased from the bottom plane to the top plane. The observed increase of the microstructural features in the direction of the ice growth is a typical characteristic of the ice-templated scaffolds and is attributed to the difficulty of maintaining a constant ice growth velocity over long distance (cm) under the unidirectional freezing conditions [71]. Note that the distance in between the bottom and top planes is 2.5 cm

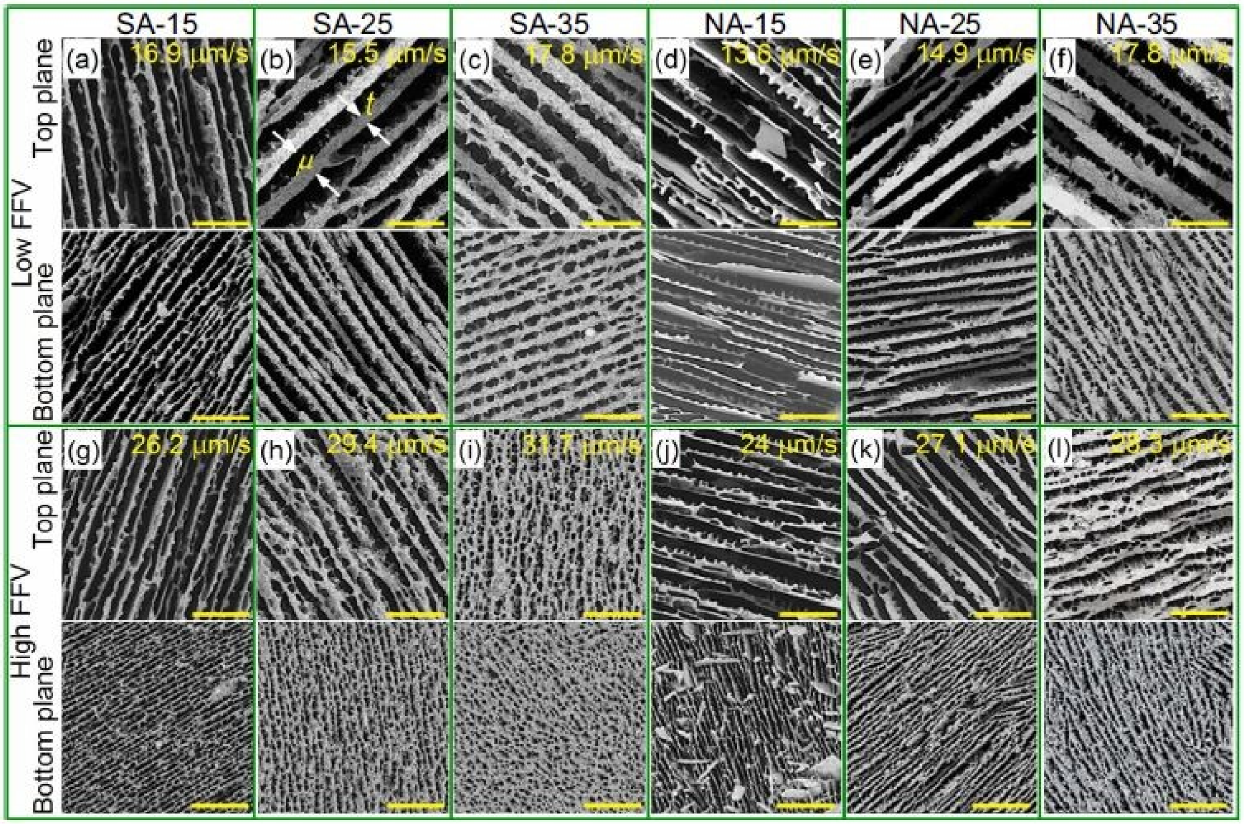

Figure 4.3: SEM micrographs of the top and bottom planes of the ice-templated Al_2O_3 scaffolds corresponding to relatively low and high freezing front velocities (FFVs). The length of the scale bar is 80 µm and ice growth direction is out of the page.

(Fig. 4.2b). A comparison among the top planes or bottom planes of the SA-scaffolds (Figs. 4.3a-c) or NA-scaffolds (Figs. 4.3d-f) at the relatively low FFVs also reveals that both the *t* and μ increase with the increasing suspension concentration, which is attributed to the increase of the solids content in the scaffolds.

Interesting microstructural differences can be noticed in between the NA-scaffolds and SA-scaffolds at the relatively high FFV regime (24-32 µm/s). For both the SA-15 (Fig. 4.3g) and SA-25 scaffolds (Fig. 4.3h) while the lamellar pattern can still be noticed, the extent of the interlamellae bridging increased significantly relative to the low FFV regime (Figs. 4.3a and 4.3b).

As a result the pore morphology rather appears dendritic [69]. For the SA-35 scaffold (Fig. 4.3i) the lamellar pore morphology is almost lost and the pores appear isotropic. Unlike the SA-scaffolds, the NA-scaffolds exhibit less marked transition of the pore morphology with the increasing FFV (Figs. 4.3j-l). It can be observed that the interlamellae bridging increased considerably with the increasing solids loading and FFV, and the pore morphology of the NA-scaffolds can be considered as dendritic at the high FFV regime. In Fig. 4.4, the high magnification SEM micrographs of the SA-35 and NA-35 scaffolds processed at the comparable high FFVs, clearly reveal that the pore morphology of the former is almost isotropic whereas it is dendritic for the later. Microstructural investigations thus suggest that the pore morphology of the SA-scaffolds gradually transitioned from a lamellar to an isotropic structure with the increasing FFV and solids loading whereas the pore morphology of the NA-scaffolds rather transitioned from lamellar to dendritic structure only. Therefore, it can be stated that within the investigated range of the FFV the ice-templated scaffolds processed from the smaller particle size NA powder preferred the

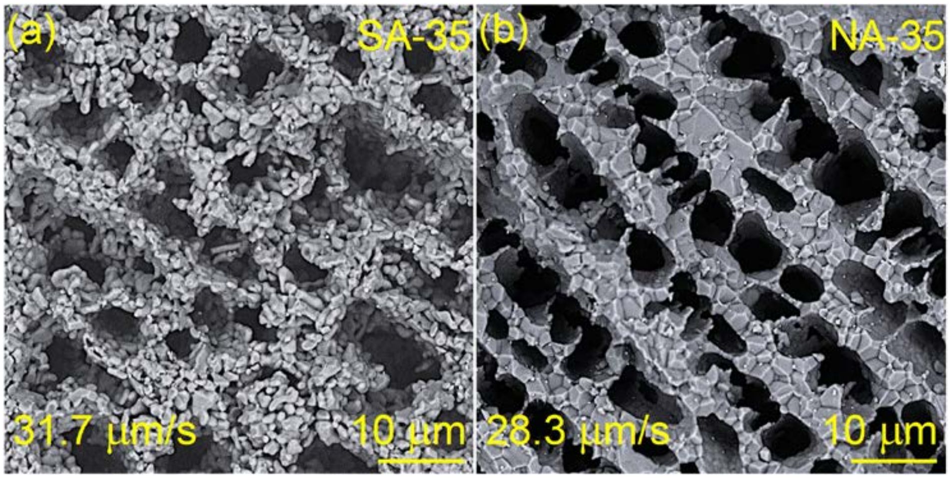

Figure 4.4: High magnification SEM micrographs revealing (a) almost isotropic pore morphology of the SA-35 scaffold and (b) dendritic pore morphology of the NA-35 scaffold processed at relatively high FFVs. Ice growth direction is out of the page.

development of the lamellar pore morphology in comparison to the scaffolds processed from the larger particle size SA powder. Critical FFV (v_c) above which the particles remain entrapped within the solvent crystals can be expressed as [52, 69],

$$v_c = \frac{\Delta\sigma d}{3\eta R}\left(\frac{a_0}{d}\right)^z \quad (1)$$

where $\Delta\sigma$ is the mean free energy of the particle, a_0 is the average intermolecular distance in the liquid film between the particle and the solid front, d is the overall thickness of this film, η is the slurry viscosity, R is the particle radius, and z is an exponent that can vary from 1 to 5. According to Equation (1) since the v_c increases with a decreasing R, a decrease of the particle size can facilitate the particle rejection by a freezing front and leads to the formation of the lamellar pore

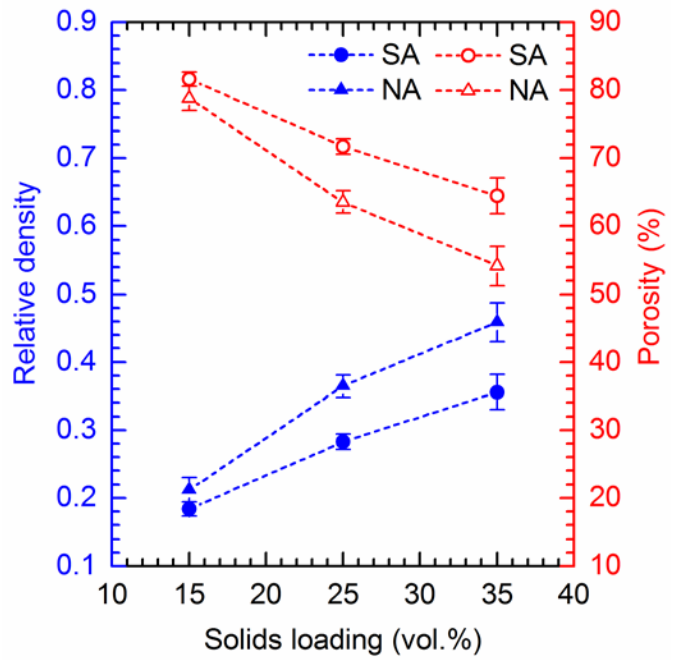

Figure 4.5: Variation of the average relative density (ρ_r) and total porosity (p_t) of NA-scaffolds and SA-scaffolds with the initial suspension concentration.

morphology. Thus, for a given suspension concentration ice-templated scaffolds tend to become relatively more lamellar with the decrease of the particle size as is also observed in this study (Figs. 4.3 and 4.4).

Figure 4.5 shows a comparison of the relative density (ρ_r) and total porosity $(p_t = (1 - \rho_r) * 100)$ of the sintered scaffolds as a function of the suspension concentration. For each composition, ρ_r and p_t values represent an average of all the sintered scaffolds processed over the FFV range investigated here. The average ρ_r and p_t values are also listed in Table 4.1. It is seen that the average ρ_r and p_t of the NA-15 is slightly higher and lower, respectively, relative to the SA-15. With the increasing suspension concentration, both the ρ_r and p_t increased and decreased, respectively. However, the NA-scaffolds exhibit a greater increase of the ρ_r (i.e., a greater decrease

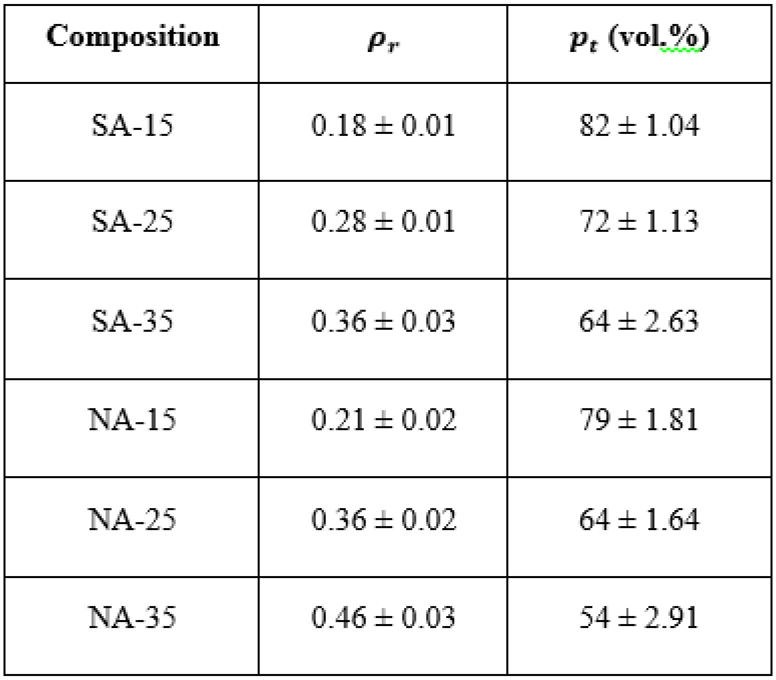

Composition	ρ_r	p_t (vol.%)
SA-15	0.18 ± 0.01	82 ± 1.04
SA-25	0.28 ± 0.01	72 ± 1.13
SA-35	0.36 ± 0.03	64 ± 2.63
NA-15	0.21 ± 0.02	79 ± 1.81
NA-25	0.36 ± 0.02	64 ± 1.64
NA-35	0.46 ± 0.03	54 ± 2.91

Table 4.1: Variation of average relative density (ρ_r) and total porosity (p_t) with solids loading.

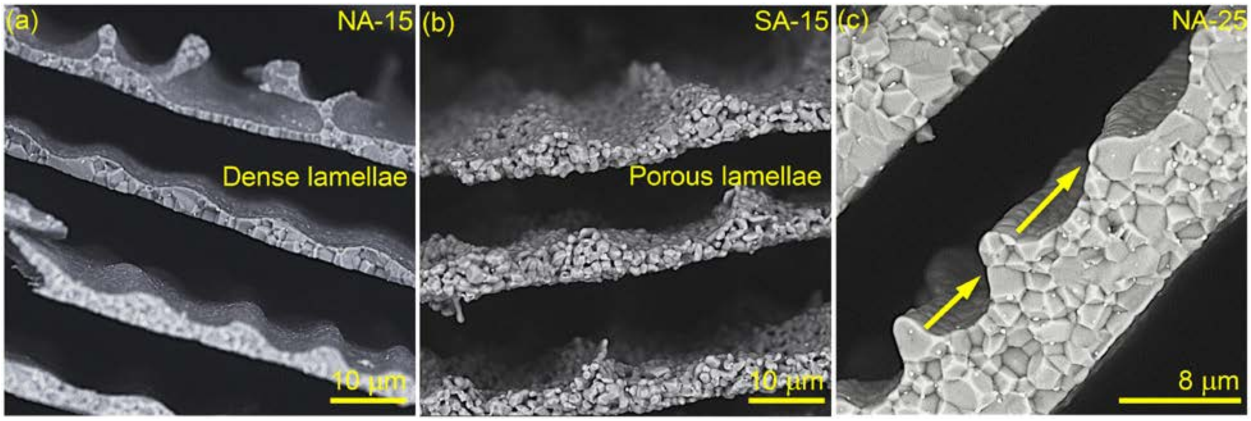

Figure 4.6: Lamellae walls microstructures of the (a) NA-15 and (b) SA-15 scaffolds revealing the dense walls for the former and porous walls for the later. (c) long-range order of the dendrites on the lamella wall of the NA-25 scaffold. Ice growth direction is out of the page.

of the p_t) in comparison to that of the SA-scaffolds. As a result, the relative difference of the ρ_r (or p_t) in between the NA-scaffolds and SA-scaffolds increased with the increasing solids loading (Fig. 4.5, Table 4.1). The observed higher ρ_r and lower p_t of the sintered NA-scaffolds relative to the SA-scaffolds can be attributed to the smaller particle size of the NA powder relative to that of the SA powder. As mentioned previously, an increase of the surface area with a decreasing particle size enhances densification of ceramics during sintering [76]. Additionally, finer particles can pack more efficiently in between the growing ice lamellae during the unidirectional freezing process in comparison to the coarser particles [75]. Figures 4.6a and 4.6b reveal the lamellae cross-sections of the sintered NA-15 and SA-15 scaffolds, respectively. It can be observed that the lamellae of the NA-15 (Fig. 4.6a) are highly dense with almost no visible porosity whereas the lamellae of the SA-15 (Fig. 4.6b) contain considerable amount of microporosity. This further supports the better sinterability of the relatively finer NA powder in comparison to the relatively coarser SA powder. Therefore, it can be stated that better particle packing within the lamellae walls and higher sinterability of the NA particles in comparison to the SA particles resulted in the higher ρ_r and thus lower p_t of the NA-scaffolds relative to that of the SA-scaffolds. Difference of the ρ_r in between the NA-scaffolds and SA-scaffolds increased progressively with the increasing solid content, which is a characteristic of ceramic sintering.

Figure 4.6 also reveals the dendritic features on one side of the lamellae walls for both the NA-15 and SA-15 scaffolds that run in the direction of ice growth; a characteristic of the ice-templated structures due to the anisotropic growth features of the ice crystals [58]. However, the dendritic surface pattern on the lamellae walls is observed to be more distinct and well developed for the NA-15 relative to the SA-15. Also, each dendrite seems to maintain a relatively long-range order

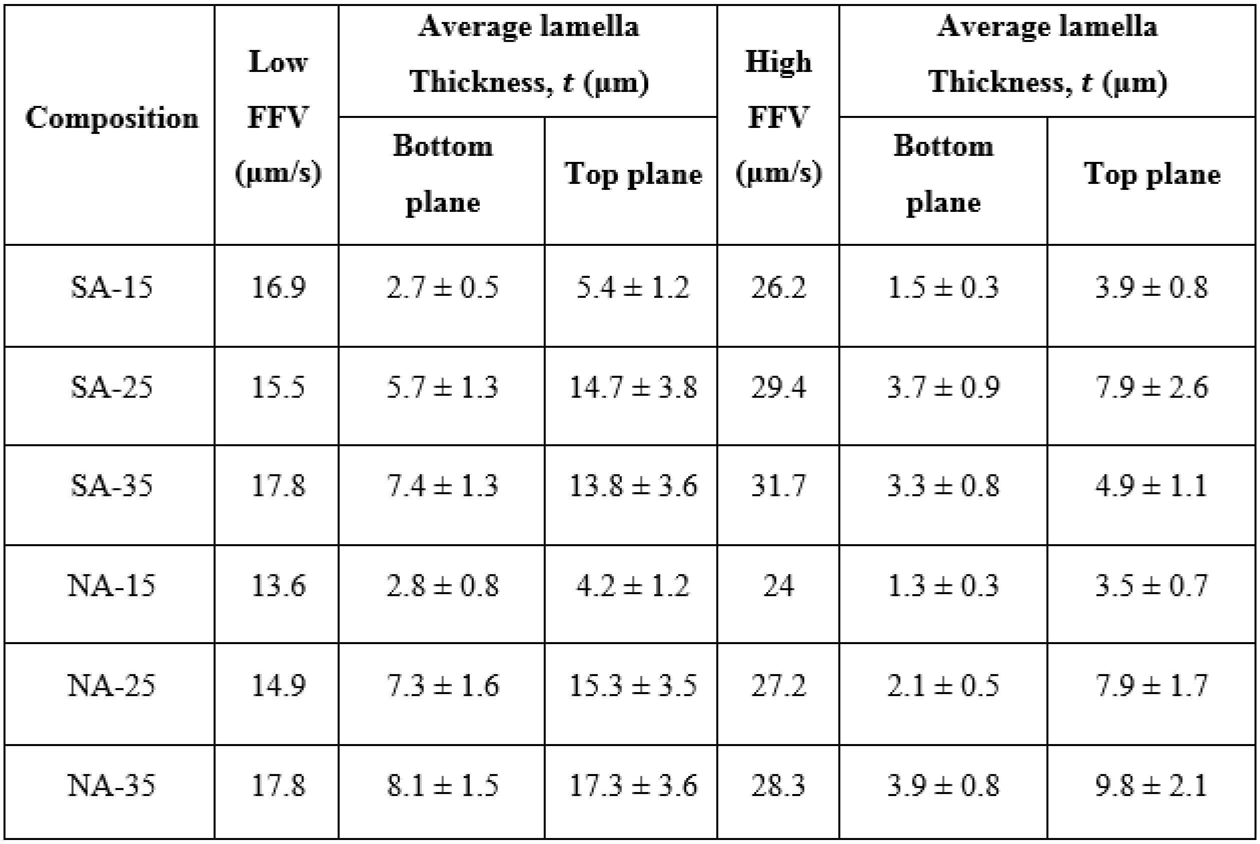

Composition	Low FFV (μm/s)	Average lamella Thickness, t (μm)		High FFV (μm/s)	Average lamella Thickness, t (μm)	
		Bottom plane	Top plane		Bottom plane	Top plane
SA-15	16.9	2.7 ± 0.5	5.4 ± 1.2	26.2	1.5 ± 0.3	3.9 ± 0.8
SA-25	15.5	5.7 ± 1.3	14.7 ± 3.8	29.4	3.7 ± 0.9	7.9 ± 2.6
SA-35	17.8	7.4 ± 1.3	13.8 ± 3.6	31.7	3.3 ± 0.8	4.9 ± 1.1
NA-15	13.6	2.8 ± 0.8	4.2 ± 1.2	24	1.3 ± 0.3	3.5 ± 0.7
NA-25	14.9	7.3 ± 1.6	15.3 ± 3.5	27.2	2.1 ± 0.5	7.9 ± 1.7
NA-35	17.8	8.1 ± 1.5	17.3 ± 3.6	28.3	3.9 ± 0.8	9.8 ± 2.1

Table 4.2: Variation of average lamella thickness (t) with solids loading and FFV.

on the lamella wall as indicated for the NA-25 scaffold in the direction of ice growth (Fig. 4.6c). Surface features observed on the lamellae walls are the direct replica of the surface morphology of the ice crystals. Due to the small size, the NA particles probably well replicated the anisotropic surface features of the ice crystals. As a result, the lamellae walls of the NA-scaffolds are observed to be significantly smoother and exhibit relatively long-range order of the dendrites in comparison to the SA-scaffolds. This can also be related to the particle size effects on the thermodynamic stability of the freezing front. Increase of the particle size causes greater supercooling effects, [74] leading to the instabilities of the freezing front [77]. Hence, the scaffolds processed from the larger particles (i.e., SA powder) can have more surface roughness compared to the scaffolds processed from the smaller particles (i.e., NA powder). Overall, the microstructural observations suggest that the particle size not only affects the pore morphology of the scaffolds but also the lamellae walls porosity and roughness.

Tables 4.2-4.5 show the variation of the average lamella thickness (t), wavelength (μ), major (a) and minor (b) axes of the pores, and pore aspect ratio ($\chi_p = a/b$), respectively, of the Al_2O_3 scaffolds corresponding to relatively low and high FFVs. Although the above microstructural parameters were not measured at the intermediate FFVs, typically these features increase gradually with the solids loading for a comparable FFV and decrease with the increasing FFV for a given solids loading [69]. Additionally, these microstructural features increase in the direction of the ice growth and substantial increase can be observed for long samples (few centimeters).[65, 71] Similar general trends can also be observed from Tables 4.2-4.5 and is not thus addressed here further. An interesting observation at the relatively high FFVs is that while the average t and μ of the NA-scaffolds increase with the solids loading, t and μ increase from SA-15 to SA-25 but decrease from SA-25 to SA-35. Since the pore morphology of the SA-35 becomes almost isotropic

Composition	Low FFV (µm/s)	Average Wavelength, μ (µm)		High FFV (µm/s)	Average Wavelength, μ (µm)	
		Bottom plane	Top plane		Bottom plane	Top plane
SA-15	16.9	12.8 ± 2.7	23.6 ± 5.8	26.2	7.7 ± 1.2	17.8 ± 3.9
SA-25	15.5	19.4 ± 5.1	41.8 ± 9.1	29.4	10.1 ± 2.1	22.3 ± 5.9
SA-35	17.8	20.1 ± 2.9	35.3 ± 8.3	31.7	8.2 ± 1.8	11.6 ± 2.1
NA-15	13.6	17.6 ± 5.3	26.3 ± 8.2	24	6.5 ± 0.7	20.5 ± 4.6
NA-25	14.9	17.8 ± 4.1	37.7 ± 7.9	27.2	7.8 ± 1.7	22.8 ± 5.4
NA-35	17.8	18.2 ± 3.5	37.7 ± 7.2	28.3	10.6 ± 2.3	23.9 ± 5.3

Table 4.3: Variation of average wavelength (μ) with solids loading and FFV.

at the high FFV, significant amount of the ceramic is consumed in forming the isotropic cells resulting in a decrease of the t and μ. This is further supported by the measured χ_p that is observed to be close to 1 for the SA-35 scaffold at the high FFV. No clear trend is observed for the χ_p in between the SA-scaffolds and NA-scaffolds at the relatively low FFVs. On the other hand, for a given composition and at the relatively high FFV, χ_p of the SA-scaffold is observed to be considerably smaller in comparison to that of the NA-scaffold (Table 4.5). Overall, the χ_p measurements also support the microstructural observations made from Figs. 4.3 and 4.4 that for a given composition and at a comparable FFV the NA-scaffold is relatively more lamellar relative to the SA-scaffolds.

Composition	Low FFV (µm/s)	Average pore major (a) and minor (b) axes (µm)				High FFV (µm/s)	Average pore major (a) and minor (b) axes (µm)			
		Bottom plane		Top plane			Bottom plane		Top plane	
		a	b	a	b		a	b	a	b
SA-15	16.9	164.7 ± 100.1	10.8 ± 3.3	261.3 ± 139.7	18.6 ± 4.7	26.2	26.1 ± 13.4	5.5 ± 0.8	189.6 ± 110.3	13.7 ± 3.1
SA-25	15.5	223.4 ± 158.3	12.3 ± 3.4	369.3 ± 189.7	24.2 ± 5.6	29.4	7.5 ± 3.3	4.3 ± 1.5	19.4 ± 11.4	8.3 ± 3.4
SA-35	17.8	37.8 ± 26.3	10.8 ± 1.9	126.3 ± 73	18.4 ± 3.5	31.7	5.0 ± 2.0	3.1 ± 1.3	8.0 ± 3.2	4.8 ± 1.9
NA-15	13.6	313.7 ± 164.4	16.2 ± 4.1	295.1 ± 134.7	24.3 ± 6.4	24	47.2 ± 24.3	6.7 ± 1.5	226.9 ± 111.7	19.9 ± 3.9
NA-25	14.9	134.3 ± 70.4	10.6 ± 1.9	247.4 ± 114.8	21.7 ± 4.5	27.2	26.9 ± 14.5	5.1 ± 1	108.3 ± 45.5	14.3 ± 2.6
NA-35	17.8	19 ± 9.0	9.1 ± 1.7	98.1 ± 58.5	18.0 ± 3.2	28.3	12.6 ± 7.7	5.4 ± 1.0	71.6 ± 50.3	12.8 ± 2.6

Table 4.4: Variation of average pore major (a) and minor (b) axes with solids loading and FFV.

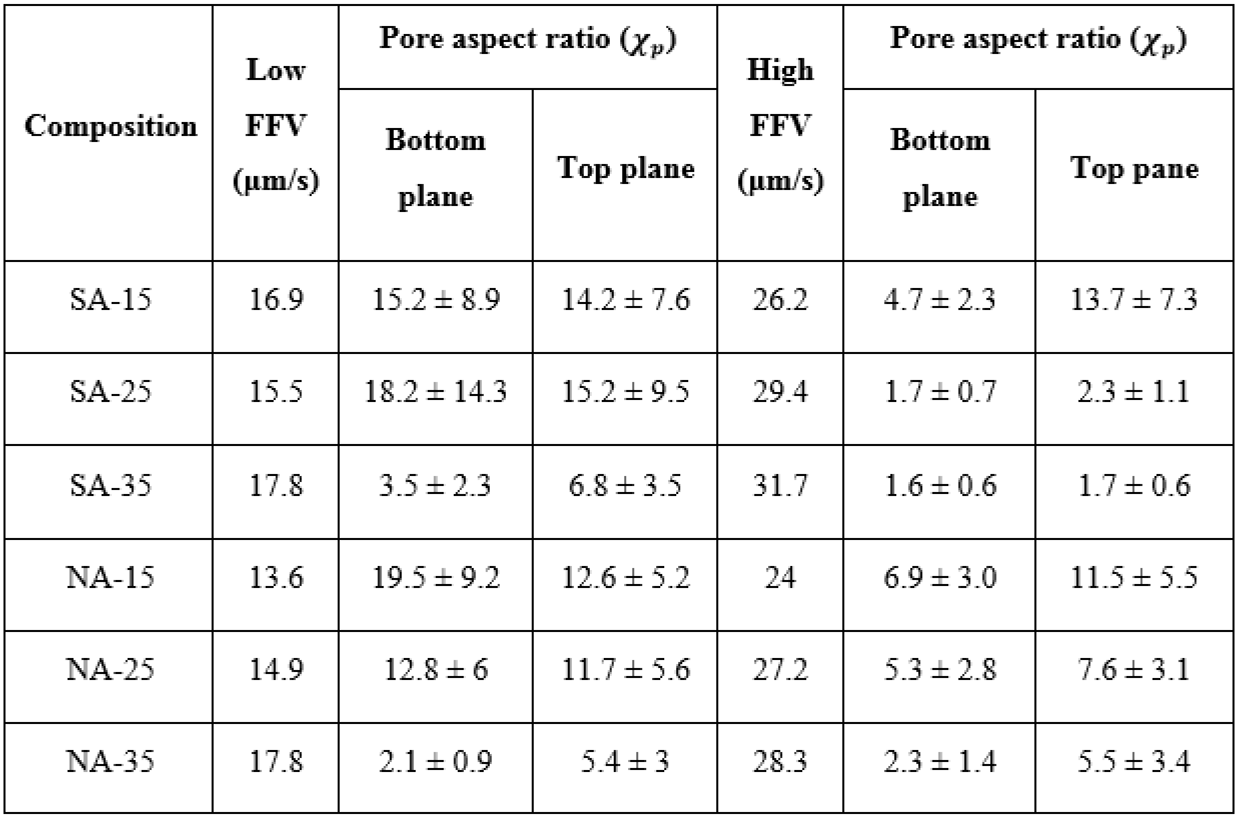

Composition	Low FFV (μm/s)	Pore aspect ratio (χ_p)		High FFV (μm/s)	Pore aspect ratio (χ_p)	
		Bottom plane	Top plane		Bottom plane	Top pane
SA-15	16.9	15.2 ± 8.9	14.2 ± 7.6	26.2	4.7 ± 2.3	13.7 ± 7.3
SA-25	15.5	18.2 ± 14.3	15.2 ± 9.5	29.4	1.7 ± 0.7	2.3 ± 1.1
SA-35	17.8	3.5 ± 2.3	6.8 ± 3.5	31.7	1.6 ± 0.6	1.7 ± 0.6
NA-15	13.6	19.5 ± 9.2	12.6 ± 5.2	24	6.9 ± 3.0	11.5 ± 5.5
NA-25	14.9	12.8 ± 6	11.7 ± 5.6	27.2	5.3 ± 2.8	7.6 ± 3.1
NA-35	17.8	2.1 ± 0.9	5.4 ± 3	28.3	2.3 ± 1.4	5.5 ± 3.4

Table 4.5: Variation of pore aspect ratio (χ_p) with solids loading and FFV.

4.2.2 Effects of freezing front velocity on relative density

Figure 4.7 presents the variation of the ρ_r of the NA-scaffolds and SA-scaffolds with the FFV. For each composition and at an FFV, the average ρ_r and standard deviation were calculated from the ρ_r values corresponding to the #1, #2 and #3 specimens. It can be observed that the ρ_r of the scaffolds increases almost linearly with the FFV except for the NA-25 where the ρ_r rather appears to decrease with the increasing FFV. For a given solids loading, the origin of the difference of the ρ_r in between the NA-scaffolds and SA-scaffolds is attributed to the finer particles size of the NA powder and is already discussed in the Section 3.1. Mass transport during the densification of the

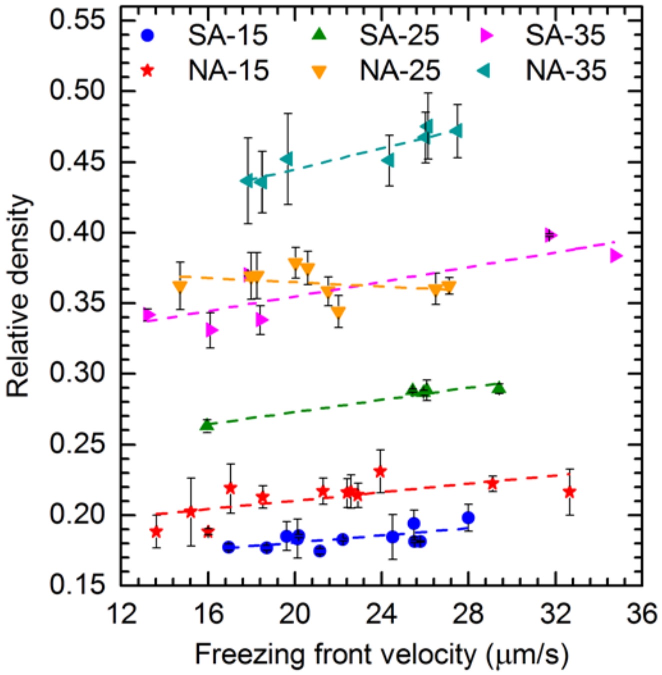

Figure 4.7: Variation of the average relative density (ρ_r) of the NA-scaffolds and SA-scaffolds with the freezing front velocity (FFV).

powder particles is enhanced by a decrease of the radius of curvature of the solid-vapor interface and, therefore, the pore radius of curvature strongly influences the density of the sintered scaffolds [69, 78]. As a result, for a given solids loading, sintered density increases with a decrease of the pore size. As discussed in the Section 3.1, for a given solids loading pore morphology of the sintered scaffolds changes with the increasing FFV due to the increase of the interlamellae bridge density (Fig. 4.3). Similarly, for a comparable FFV, the pore morphology also changes with the increasing solids loading (Fig. 4.3). Overall, with the increasing FFV and solids loading, pore morphology gradually transitions from lamellar to almost isotropic for the SA-scaffolds and lamellar to dendritic for the NA-scaffolds. As a result, both the average pore size (Table 4.4) and the aspect ratio (Table 4.5) decrease with the increasing FFV and solids loading. Since, the dendritic and isotropic pores have a smaller radius of curvature in comparison to the lamellar pores

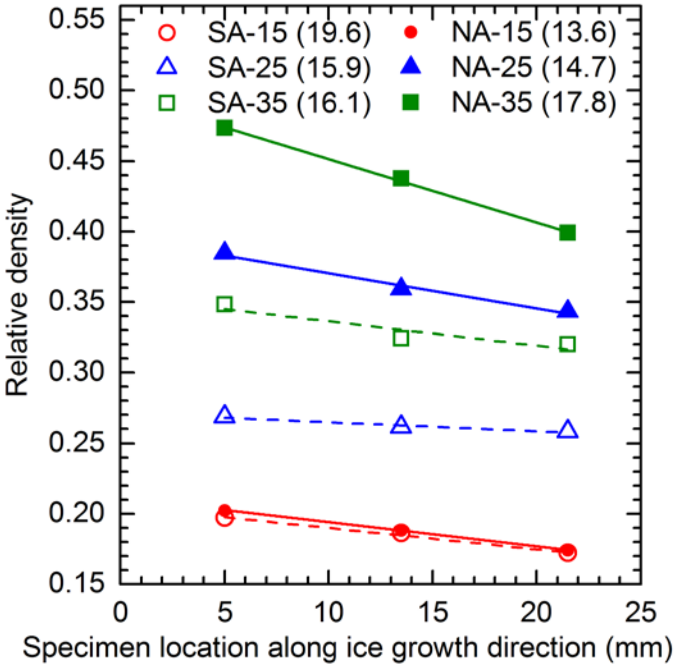

Figure 4.8: Variation of the relative density within the SA-scaffolds and NA-scaffolds along the direction of the ice growth. For each composition, average FFV value is also provided.

that are large and flat, an increase of the sintered density will result as the pores become increasingly dendritic/isotropic. Figure 4.8 shows the variation of the ρ_r of the #1, #2 and #3 specimens (Figure 4.2b) of the NA-scaffolds and SA-scaffolds processed at the comparable FFVs. For a given composition, ρ_r decreases slightly from the #1 to #2 to #3 specimens and a similar trend is observed at all other FFVs also (not shown here). It can be noticed that over a large sample length of approximately 21 mm, variation of the ρ_r is only about 0.02-0.04 (2-4% porosity) except for the NA-35 that exhibits a variation of the ρ_r of about 0.07 (7% porosity). Figure 4.8 also suggests that the overall structural gradient remains comparable irrespective of the particle size.

4.2.3 Uniaxial compressive fracture strength

Having discussed the effects of the variation of the particle size on the microstructure and ρ_r, the

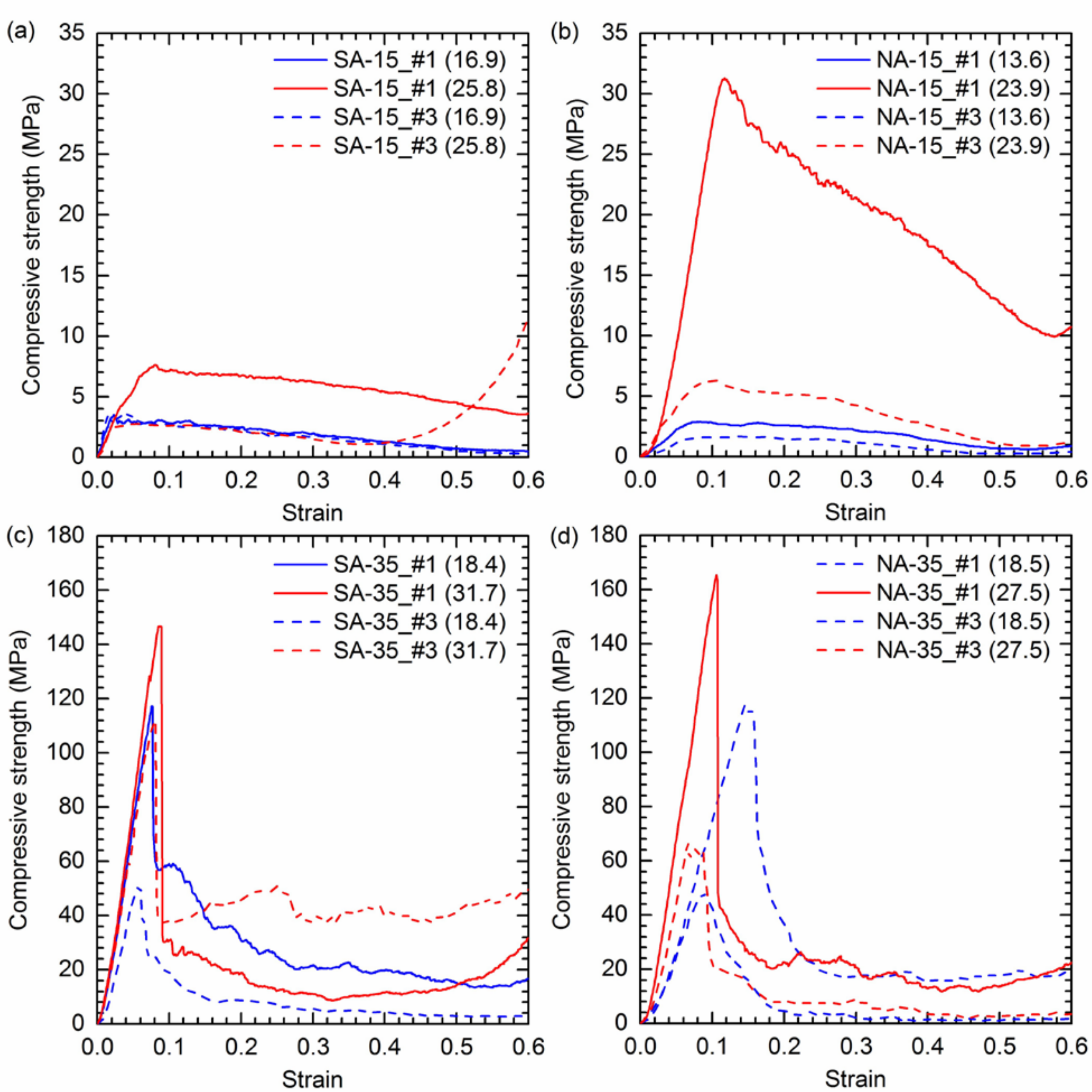

Figure 4.9: Representative stress-strain curves of the (a) SA-15 scaffold, (b) NA-15 scaffold, (c) SA-35 scaffold, and (d) NA-35 scaffold corresponding to the relatively low and high FFVs. For each composition and FFV, compressive response of the #1 and #3 specimens are shown up to a strain level of 0.6, after which densification started.

results of the uniaxial compressive strength measurements are now discussed here. Figure 4.9 shows the representative stress-strain curves of the SA-15 (Fig. 4.9a), NA-15 (Fig. 4.9b), SA-35 (Fig. 4.9c), and NA-35 (Fig. 4.9d) scaffolds corresponding to the relatively low and high FFVs. For each composition and FFV, compressive response of the #1 and #3 specimens are shown up to a strain level of 0.6, after which densification started. For a given composition and FFV, compressive strength of the #1 specimen is always observed to be greater in comparison to that of the #3 specimen. Although not shown for clarity but the strength of the #2 specimen appears in between that of the #1 and #3. The decrease of the strength from #1 to #2 to #3 can be attributed to the decrease of the ρ_r in the same sequence within a scaffold (Fig. 4.8). As mentioned earlier, the decrease of the ρ_r from the bottom to the top of a scaffold is due to the gradual change of the pore morphology and/or pore size, where the pore size and aspect ratio increases along the ice growth direction (Fig. 4.3, Tables 4.4 and 4.5). Thus, the observed decrease of the compressive strength from #1 to #2 to #3 specimens of a scaffold can also be attributed to the increase of the pore size and aspect ratio along the ice growth direction. Additionally, for a given composition strength of the #1 (or #3) increases with the FFV. Recall from Figure 4.7 that for a given scaffold composition ρ_r increases with the FFV due to the decrease of the pore size with the increasing FFV. Therefore, the observed increase of the strength of the #1 (or #3) with the FFV for a given composition is attributed to the combined effects of the increase of the ρ_r and decrease of the pore size and aspect ratio with the increasing FFV.

It can be further observed that the SA-15 (Fig. 4.9a) and NA-15 (Fig. 4.9b) scaffolds exhibit comparable compressive strength values (<10 MPa) except the #1 specimen of the NA-15 at high FFV that shows a significantly higher value (~31 MPa). In fact, for all the NA-15 scaffolds processed at the relatively high FFVs strength of the #1 specimens is observed to be significantly

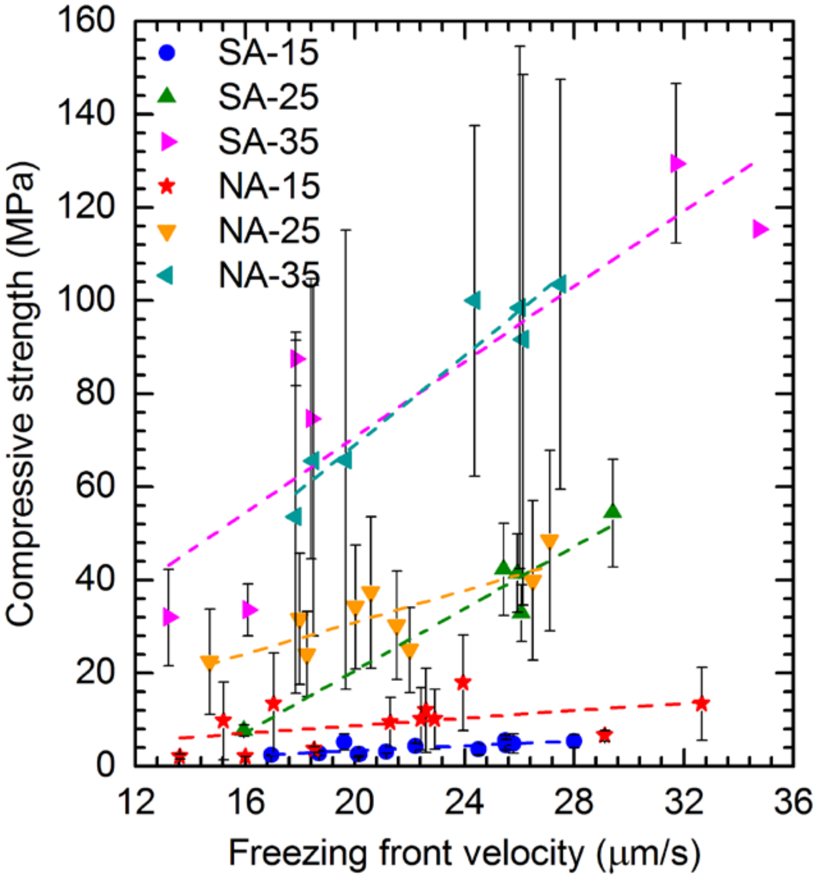

Figure 4.10: Variation of the compressive fracture strength of SA-scaffolds and NA-scaffolds with the FFV.

higher in comparison to that of the #2 and #3 specimens. Increase of the strength with the increasing suspension concentration is attributed to decrease of the porosity (Fig. 4.5, Table 4.1). Additionally, some characteristic differences of the stress-response can be noticed in between the high porosity (SA-15 and NA-15) and low porosity scaffolds (SA-35 and NA-35). Stress-strain curves of the SA-15 and NA-15 scaffolds suggest the occurrence of the progressive failure under the compressive loading conditions as is evidenced by the gradual decrease of the stress with the increasing strain, a typical cellular-like response of the highly porous solids [3, 36, 65]. In contrast, the SA-35 and NA-35 scaffolds exhibit a sudden drop of the stress once the peak stress is achieved indicating a significant decrease of the load-bearing capacity that is a typical characteristic of the brittle-like failure.

Figure 4.10 compares the variation of the average compressive strength of the Al_2O_3 scaffolds as a function of the FFV. For each composition and at a FFV, the average strength and standard deviation were calculated from the strength values of the #1, #2 and #3 specimens. Although significant scatter of the data is observed particularly for the scaffolds with the higher solids loadings, the average compressive strength for a given composition increases almost linearly with the FFV. Also, all the six scaffold compositions can be divided in to three groups in terms of the observed variation of the strength with the FFV: (i) SA-15 and NA-15, (ii) SA-25 and NA-25, and (iii) SA-35 and NA-35. Within each group, in general, both the SA-scaffold and NA-scaffold exhibit comparable strength values as a function of the FFV. While this observed trend could be expected for the SA-15 and NA-15 scaffolds since their ρ_r values are marginally different (Figs. 4.5 and 4.7, Table 4.1), the NA-25 and NA-35 scaffolds are expected to exhibit markedly greater compressive strength in comparison to the SA-25 and SA-35 scaffolds, respectively. This is because both the NA-25 and NA-35 scaffolds have significantly higher ρ_r (thus lower p_t) in comparison to that of the SA-25 and SA-35 scaffolds, respectively (Figs. 4.5 and 4.7, Table 4.1). Overall, Fig. 4.10 reveals that the compressive strength of the ice-templated scaffolds is significantly influenced by the FFV and suspension concentration. Moreover, for a given suspension composition and at a comparable FFV, while the microstructure (Fig. 4.3) and ρ_r (Fig. 4.7) are significantly influenced by the particle size variation, effects of the particle size variation on the compressive strength appear to be marginal.

To provide further insights into the compressive response of the scaffolds, in Fig. 4.11 the variation of the strength with the ρ_r is shown. For each composition, the strength values of the #1, #2 and

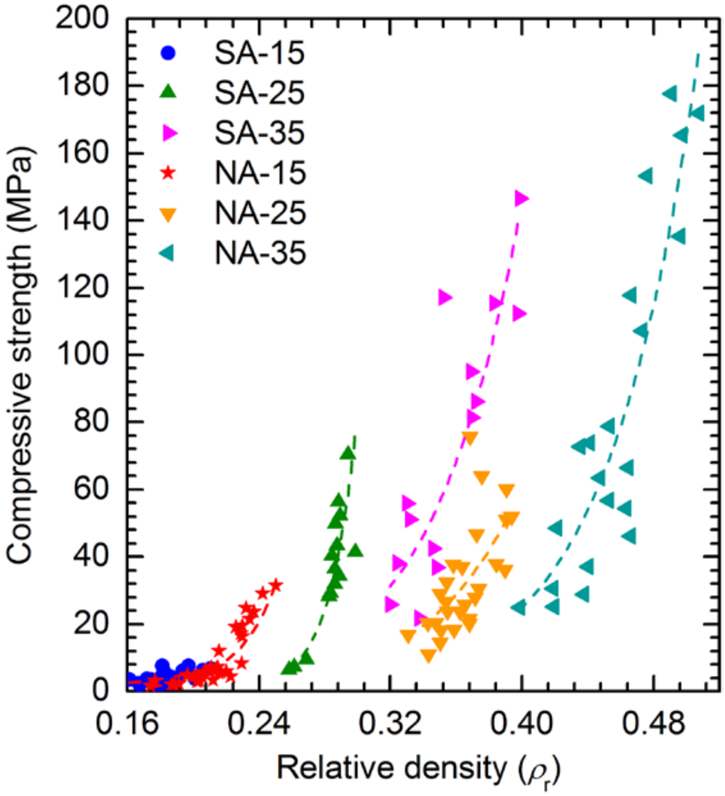

Figure 4.11: Variation of the compressive fracture strength of the SA-scaffolds and NA-scaffolds with the relative density (ρ_r).

#3 specimens of all the scaffolds processed within the investigated range of the FFVs are included. The observed variation of the ρ_r for each composition originates from the variation of the ρ_r with the FFV (Fig. 4.7). For the SA-15 and NA-15 scaffolds, while the compressive strength increases slightly with the ρ_r, strength values of both the scaffolds are observed to be low. Except the #1 specimens of the NA-15 scaffolds processed at the high FFVs that exhibit compressive strength in the range of 15-30 MPa, overall strength of the SA-15 and NA-15 scaffolds is observed to be comparable and below 10 MPa. Since the ρ_r of the SA-15 and NA-15 scaffolds are slightly different, it can be stated that the strength is mainly governed by the ρ_r. Interestingly, a different trend is observed at the higher solids loadings. The compressive strength of both the SA-25 and

NA-25 scaffolds is observed to be comparable and within a range of 10 to 80 MPa. Figure 4.11 thus suggests that in spite of having an approximately 8% difference of the average ρ_r (Table 4.1) strength values of both the SA-25 and NA-25 scaffolds fall almost within the same range. In other words, for both the scaffolds comparable strength values can be found that correspond to the sintered specimens with a ρ_r difference of about 8%. A similar trend is also exhibited by the SA-35 and NA-35 scaffolds where the strength increased significantly with the ρ_r and both the scaffolds exhibit comparable strength values but at a ρ_r difference of about 10%. The observed increase of the strength with the ρ_r for each scaffold composition is consistent with the known trend that strength of the cellular solids increases with the ρ_r. [3] However, the comparable strength of the SA-25 and NA-25 (or SA-35 and NA-35) scaffolds but at distinctly different ρ_r strongly suggests that the ρ_r does not solely govern the compressive response. This is because while a higher ρ_r of the NA-25 in comparison to the SA-25 (or NA-35 in comparison to SA-35) would increase the strength of the former than the later, it is possible that there are certain microstructural features that enhanced the strength of the SA-25 in comparison to the NA-25 (or of SA-35 in comparison to NA-35). As a result, both the SA-25 and NA-25 scaffolds (or SA-35 and NA-35) exhibit comparable strength but at widely different ρ_r.

Recall from Fig. 4.3 that for a given suspension concentration and at a comparable low or high FFV, the NA-scaffolds are observed to be relatively more lamellar (or less dendritic/isotropic) in comparison to the SA-scaffolds. For example, the pore morphology of the SA-35 changed from lamellar at relatively low FFV (Fig. 4.3c) to almost isotropic at relatively high FFV (Fig. 4.3i). However, within the comparable range of the FFV, pore morphology of the NA-35 rather transitioned from lamellar (Fig. 4.3f) to dendritic structure (Fig. 4.3l). As discussed previously, the observed microstructural differences in between the SA-scaffolds and NA-scaffolds within the investigated range of the FFVs are attributed to the particle size effects on the particle rejection/entrapment by an advancing ice front. Here in addition to the ρ_r, the microstructural differences in between the SA-scaffolds and NA-scaffolds have a crucial influence on the observed compressive response. This is because for the freeze-cast ceramic scaffolds, in addition to the ρ_r, pore aspect ratio (χ_p) and interlamella bridge density (ρ_b) influence the mechanical properties [61, 65]. ρ_b is defined as the number of ceramic bridges in between the adjacent lamellae per unit area [69]. It has been shown that as the pore morphology of the scaffolds transitions from a lamellar to dendritic/isotropic structure, both the pore size and χ_p decrease, which, in turn, increases the number of bridges in between the adjacent ceramic lamellae. The compressive load-bearing capacity of the scaffolds particularly in the direction of the ice growth is thus enhanced with the decreasing pore size and χ_p, i.e., with the increasing ρ_b, and hence the compressive fracture strength. Based on the above discussion, the variations of the key strength governing factors such as the ρ_r, χ_p, and ρ_b in between the SA-scaffolds and NA-scaffolds are utilized to rationalize the observed relationships of the compressive strength vs. FFV (Fig. 4.10) and compressive strength vs. ρ_r (Fig. 4.11).

Figure 4.12 shows variations of the average ρ_r, average χ_p, and ratio of the average ρ_b of the SA-scaffolds and NA-scaffolds ($\rho_{b(SA)}/\rho_{b(NA)}$) with the solids loading. For each composition, ρ_r, χ_p, and ratio of the ρ_b values are shown for a representative scaffold fabricated at a relatively high FFV to mainly rationalize the upper bound of the measured compressive strength values. It is note that estimation of these quantities at all the FFVs for all the compositions is beyond the scope of this study. For each representative scaffold, average ρ_r shown in Fig. 4.12a was estimated from the #1, #2 and #3 specimens. Similarly, for each representative scaffold, average χ_p value shown in Fig. 4.12b is the average of the pore aspect ratio of the bottom and top planes. For the

$\rho_{b(SA)}/\rho_{b(NA)}$ (Fig. 4.12c), first the average ρ_b of the each representative scaffold was determined from the ρ_b values of the bottom and top planes. Next, for a given solids loading, $\rho_{b(SA)}/\rho_{b(NA)}$ was determined from the average ρ_b values of the SA-scaffold and NA-scaffold. Figure 4.12a shows that for each solids loading ρ_r of the NA-scaffold is higher than that of the SA-scaffold, which is expected to enhance the strength of the former compared to the later. Although a large scatter can be noticed for the χ_p (Fig. 4.12b, Table 4.5), the SA-scaffold and NA-scaffold at 15 vol.% solids loading exhibit comparable values. Whereas at other solids loadings, χ_p of the SA-scaffold is observed to be considerably smaller compared to that of the NA-scaffold. Figure 4.12c shows that at all the three solids loadings $\rho_{b(SA)}/\rho_{b(NA)}$ remains consistently greater than 1, suggesting that the average ρ_b of the SA-scaffold is greater than that of the NA-scaffold for the

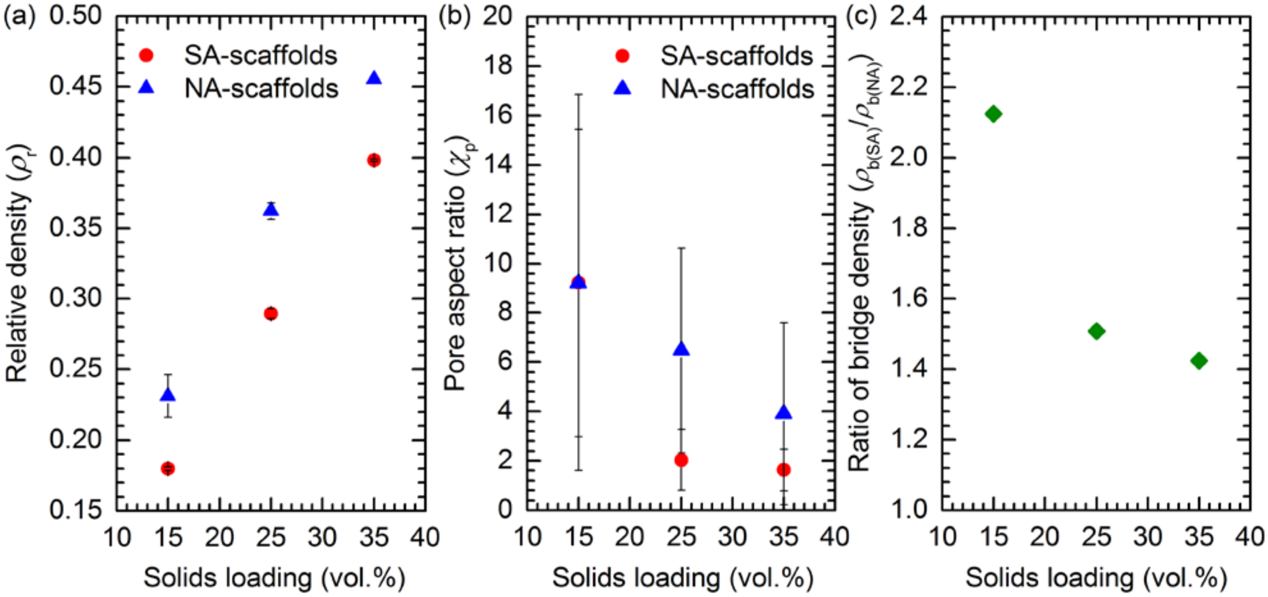

Figure 4.12: Variations of the (a) average ρ_r, (b) average χ_p, and (c) $\rho_{b(SA)}/\rho_{b(NA)}$ of the SA-scaffolds and NA-scaffolds with the solids loading. All the scaffolds were processed at high FFVs.

comparable solids loading and FFV. As discussed previously, the decrease of the χ_p and the increase of the ρ_b is expected to enhance the strength of the ice-templated scaffolds. Figure 4.12 thus suggests that there are opposing factors that contribute to the strength of the SA-scaffolds and NA-scaffolds. While the ρ_r tends to increase the compressive strength of the NA-scaffolds over that of the SA-scaffolds, χ_p and ρ_b would tend to enhance the strength of the SA-scaffolds over that of the NA-scaffolds. It is thus possible that for a comparable solids loading and FFV, these parameters balance out in a way that the compressive strength of the SA-scaffolds and NA-scaffold become comparable as is observed in Figs. 4.10 and 4.11. As a result, while the effects of the variation of the particle size on the microstructure of the ice-templated scaffolds are significant (Fig. 4.3), effects of the particle size variation on the compressive strength are observed to be marginal.

Although there is no single comprehensive study on the particle size effects on the compressive strength of the freeze-cast sintered scaffolds, Deville et al. [71] recently conducted a meta-analysis of the influence of the starting particle size on the compressive strength by combining data for various materials and solvents. In spite of a significant scatter of the data and different materials used, the meta-analysis interestingly revealed that the upper bound of the compressive strength is comparable within a particle size range of 0.5-2 μm, which is similar to the results observed in this study. It is notable that freeze casting is a physical process and the dependence on the powder material type is not expected to be significant. Therefore, it is suggested that the current investigation sheds some light on the results of the meta-analysis of the particle size vs. strength by Deville et al. [71] and provides a rationale for the observed comparable upper bound of the strength within the particle size range of 0.5-2 μm. Another important implication of the present study is that the particle size variation within a range of submicrometer to few micrometers (typical particle size range used in ceramic processing) can be uniquely employed to systematically modify the microstructure of the ice-templated ceramic scaffolds, however, without significantly altering their compressive response; which, can be useful to optimize the structure-property relationships of the ice-templated scaffolds for the structural, biomedical and functional applications.

4.3 CONCLUSIONS

In this investigation, ice-templated Al_2O_3 scaffolds were fabricated from two different particle sizes (0.3 μm, NA powder and 0.9 μm, SA powder) at three different solids loadings (15, 25, and 35 vol.%) and within a FFV range of 12-34 $\mu m/s$. For both the SA-scaffolds and NA-scaffolds, relative density and total porosity increased and decreased, respectively, with the increasing solids loading. However, the increase was observed to be significantly greater for the NA-scaffolds relative to the SA-scaffolds. For each scaffold composition, the relative density also increased with the increasing FFV. The pore morphology of both the SA-scaffolds and NA-scaffolds changed with the increasing solids loading and FFV. However, it was observed that with the increasing solids loading and FFV while the pore morphology of the SA-scaffolds transitioned from a lamellar to an almost isotropic structure, the NA-scaffolds only transitioned from lamellar to dendritic structure. The observed microstructural differences due to the particle size variation are rationalized based on the interactions of the powder particles with the freezing front during the unidirectional ice-templating process, where the smaller particles are rejected by the ice fronts with a relative ease in comparison to the larger particles. As a result, the smaller particles exhibit a better tendency to develop a lamellar pore architecture relative to the larger particles. Uniaxial compressive stress-strain measurements, however, revealed marginal variations of the strength in between the SA-scaffolds and NA-scaffolds in spite of the significant differences of the microstructure and the relative density at a comparable solids loading and FFV. The apparent marginal particle size effects on the compressive strength are rationalized based on the relative variation of the relative density, pore aspect ratio, and interlamellae bridge density in between the SA-scaffolds and NA-scaffolds. This study also suggests that within a particle size range of submicrometer to few micrometers, it could be possible to develop ice-templated ceramic scaffolds of considerably different microstructures, however, of comparable compressive strength which may find applications in the structural, bio-medical, impact energy absorption and energy storage fields.

4.4 FUTURE WORK

The data presented in this study show strong trends in terms of effects of varying the size of the ceramic particles, on the microstructure and relative density of the icetemplated sintered scaffolds. However, in spite of the observed differences of the microstructure, relative density, and porosity, the uniaxial compressive stress-strain measurements revealed marginal particle size effects on the compressive strength of the sintered scaffolds. Thus, the current investigation sheds some light on the results of the meta-analysis of the particle size vs. strength by Deville et al. [71] and provides a rationale for the observed comparable upper bound of the strength within the particle size range of 0.5-2 μm, based on the relative variation of the relative density, pore aspect ratio, and interlamellae bridge density in between the sintered alumina scaffolds processed from 0.3 μm and 0.9 μm particle sizes. As a result, analyzing and understanding these effects over a larger range of particle sizes (from few nanometers to few micrometers), could be worthy of future investigations to provide further insight into the process-structure-property relationships of freeze-cast cellular ceramics. A thorough understanding of the relationships between the rheological properties of the initial suspension and the final characteristics of the porous structures and corresponding mechanisms in freezing process, with respect to the varying powder particle size, is still at an early stage; hence, further investigation involving these aspects may be helpful in evolving stronger and tougher, light weight ceramic architectures.

REFERENCES

[1] W. D. Callister Jr., and D. G. Rethwisch, *Materials science and engineering an introduction*, eighth edition, John Wiley & Sons, Inc. USA, 2010.

[2] Liu Gang, *Fabrication of porous ceramics and composites by a novel freeze casting process*, Ph. D. thesis, University of Birmingham, 2011.

[3] L. J. Gibson and M. F. Ashby, *Cellular solids: Structures and properties*, Second edition Cambridge University Press, Cambridge, UK, 1997.

[4] N. Ni, S. Barg, E. G. Tunon, F. M. Perez, M. Miranda, C. Lu, C. Mattevi, and E. Saiz, *Understanding mechanical response of elastomeric graphene networks,* Scientific Reports, 2015, 5, 1-14.

[5] P. Colombo, *Conventional and novel processing methods for cellular solids*, Philosophical Transactions of the Royal Society A, 2006, 364, 109-124.

[6] A. Vahidifar, S. N. Khorasani, C. B. Park, H. E. Naguib, H. A. Khonakdar, *Fabrication and characterization of closed cell rubber foams based on natural rubber/carbon black by one step foaming process,* Industrial & Engineering Chemistry Research, 2016, 55, 2407-2416.

[7] J. Luyten, S. Mullens, J. Cooymans, A. M. De Wilde, I. Thijs, and R. Kemps, *Different methods to synthesize ceramic foams*, Journal European Ceramic Society, 2009, 29, 829-832.

[8] J. Luyten, S. Mullens, J. Cooymans, A. M. De Wilde, and I. Thijs, *New processing techniques of ceramic foams*, Journal of Advanced Engineering Materials, 2003, 5, 715-718.

[9] S. Sharafat, N. Ghoniem, M. Sawan, A. Ying, and B. Williams, *Breeder foam: An innovative solid breeder material for fusion application*, Journal of American Ceramic Society, 2006, 81, 455-460.

[10] S. Dhara, and P. Bhagarva, A simple direct casting route to ceramic foams, Journal of American Ceramic Society, 2003, 86, 1645-1650.

[11] S. Ahmad, M. A. Latif, H. Taib, and A. F. Ismail, *Short review: Ceramic foam fabrication techniques for wastewater treatment application,* Advanced Materials Research, 2013,795, 5-8.

[12] M. F. Ashby, *Properties of foams and lattices*, Philosophical Transactions of the Royal Society A, 2006, 364, 15-30.

[13] R. Bouix, P. Viot, and J. L. Lataillade, *Polypropylene foam behavior under dynamic loadings: strain rate, density and microstructure effects*, International Journal of Impact Engineering, 2009, 36, 329-342.

[14] J. L. Yu, J. R. Li, and S. S. Hu, *Strain rate effect and microstructural optimization of cellular metals,* Mechanics of materials, 2006, 38, 160-170.

[15] M. Virul, and G. Ravichandran, *Dynamic response and energy dissipation characteristics of balsa wood: Experiment and analysis*, International Journal of Solids and Structures, 2003, 40, 2147-2170.

[16] G. Subhash, Q. Liu, and X. L. Gao, *Quasistatic and high strain rate uniaxial compressive response of polymeric structural foams,* International Journal of Impact Engineering, 2006, 32, 1113-1126.

[17] S.Y. Shan, J.F. Yang, and J.Q. Gao, *Porous silicon nitride ceramics prepared by reduction–nitridation of silica*, Journal of the American Ceramic Society, 2005, 88, 2594-2596.

[18] I. H. Arita, V. M. Castano, and D. S. Wilkinson, *Synthesis and processing of hydroxyapatite ceramic tapes with controlled porosity*, Journal of Materials Science: Materials in Medicine, 1995, 6, 19–23.

[19] A.R. Studart, U.T. Gonzenbach, and E. Tervoort, *Processing routes to macroporous ceramics: a review,* Journal of the American Ceramic Society, 2006, 89, 1771-1789.

[20] M. Scheffler, and P. Colombo, *Cellular ceramics: structure, manufacturing, properties and applications*, Weinheim, Wiley-VCH, 2005.

[21] K. Schwartzwalder and A.V. Somers, *Methods of making porous ceramic articles*, US patent, No.3090094, May 21 1963.

[22] P. Colombo and J. R. Hellmann, *Ceramic foams from preceramic polymers*, Material Research Innovations, 2002, 6, 260–272.

[23] M. D. M. Innocentini, P. Sepulveda, V. R. Salvini, V. C. Pandolfelli, and J. R. Coury, *Permeability and structure of cellular ceramics: A comparison between two preparation techniques*, Journal of the American Ceramic Society, 1998, 81, 3349–3352.

[24] P. Sepulveda, *Gelcasting Foams for Porous Ceramics*, American Ceramic Society Bulliten, 1997, 76. 61–65.

[25] A. Imhof and D. J. Pine, *Preparation of titania foams*, Journal of Advanced Materials, 1999, 11, 311–314.

[26] Y. Hotta, P. C. A. Alberius, and L. Bergstrom, *Coated polystyrene particles as templates for ordered macroporous silica structures with controlled wall thickness*, Journal of Materials Chemistry, 2003, 13, 496–501.

[27] S. R. Mukai, H. Nishihara, and H. Tamon, *Formation of monolithic silica gel microhoneycombs (SMHs) using pseudosteady state growth of microstructural ice crystals*, Chemical Communications, 2004, 7, 874–875.

[28] K. Araki, and J. W. Halloran, *Porous ceramic bodies with interconnected pore channels by a novel freeze casting technique*, Journal of the American Ceramic Society, 2005, 88, 1108–1114.

[29] P. Colombo, E. Bernardo, and L. Biasetto, *Novel microcellular ceramics from a silicone resin*, Journal of the American Ceramic Society, 2004, 87, 152–154.

[30] O. Lyckfeldt and J. M. F. Ferreira, *Processing of porous ceramics by starch consolidation*, Journal of the European Ceramic Society, 1998, 18, 131–140.

[31] T. J. Fitzgerald, V. J. Michaud, and A. Mortensen, *Processing of microcellular SiC foams. 2. Ceramic foam production*, Journal of Materials Science, 1995, 30, 1037–1045.

[32] C. G. Anestrus, W. Schärfl, and B. Ullrich, *Microstructure evaluation of* Al_2O_3 *ceramics with Mg-PSZ- and* TiO_2*-additions*, Journal of the European Ceramic Society, 2007, 27, 3191-3199.

[33] D. J. Green, *Fabrication and mechanical properties of lightweight ceramics produced by sintering of hollow spheres*, Journal of American Ceramic Society, 1985, 68, 403-409.

[34] W. S. Sanders, and L. J. Gibson, *Mechanics of hollow sphere foams*, Materials Science and Engineering A, 2003.

[35] A. Weist, C. A. MacDougall and R. D. Conner, *Optimization of cellular solids for energy absorption*, Scripta Materialia, 2014, 84-85, 7-10.

[36] D. Ghosh, A. Wiest, and R. D. Conner, *Uniaxial quasistatic and dynamic compressive response of foams made from hollow glass microspheres*, Journal of the European Ceramic Society, 2015.

[37] B. Y. Tay, J. R. G. Evans, and M. J. Edirsinghe, *Solid free form fabrication of ceramics*, International Materials Reviews, 2003, 48, 341-370.

[38] H. Seitz, W. Rieder, and S. Irsen, *Three-dimensional printing of porous ceramic scaffolds for bone tissue engineering*, Journal of Biomedical Materials Research Part B: Applied Biomaterials, 2005, 74, 782-788.

[39] Gibson, Ian, and Jorge Bártolo, Paulo, *Stereolithography: Materials, processes, and applications*, 2011, XII, Springer Science+Business Media, LLC, 41-43.

[40] C. Deckard, *Method and apparatus for producing parts by selective sintering*, U.S. Patent 4,863,538, filed October 17, 1986, published September 5, 1989.

[41] J. Butt, H. Mebrahtu and H. Shirvani, *Rapid prototyping by heat diffusion of metal foil and related mechanical testing*, International Journal of Advanced Manufacturing Technology, 2016, 84, 2357–2366.

[42] A. Tsouknidas, M. Pantazopoulos, I. Katsoulis, D. Fasnakis, S. Maropoulos and N. Michailidis, *Impact absorption capacity of 3D-printed components fabricated by fused deposition modelling*, Materials & Design, 2016, 102, 41–44.

[43] G. McKerricher, D. Titterington, and A. Shamim, *A fully ink-jet printed 3-D honeycomb inspired patch antenna*, IEEE antennas and wireless propagation letters, 2016, 15, 544-547.

[44] Hue P. Le and Le Technologies, Inc., Beaverton, Oregon, *Progress and trends in ink-jet printing technology*, Journal of Imaging Science and Technology, 42, 1998, 49 - 62.

[45] T. Moritz and H. J. Richter, *Ceramic bodies with complex geometries and ceramic shells by freeze casting using ice as mold material*, Journal of the American Ceramic Society, 2006, 89, 2394-2398.

[46] M. J. Statham, F. Hammett, and B. Harris, *Net-shape manufacture of low-cost ceramic shapes by freeze-gelation*, Journal of Sol-Gel Science and Technology, 1998, 13, 171-175.

[47] S. Deville, E. Saiz, R. K. Nalla, and A. P. Tomsia, *Freezing as a path to build complex composites*, Science, 2006, 311, 515-518.

[48] H. Zang, I. Hussain, M. Brust, M. F. Butler, S. P. Runnard, and A. I. Cooper, *Aligned two and three dimensional structures by directional freezing of polymers and nanoparticles*, Nature Materials, 2005, 4, 787-793.

[49] D. R. Uhlman, B. Chalmers, and K. A. Jackson, *Interaction between particles and a solid-liquid interface*, Journal of Applied Physics, 1964, 35, 2986-2992.

[50] T. Waschkies, R. Oberacker, and M. J. Hoffmann, *Investigation of structure formation during freeze-casting from very slow to very fast solidification velocities*, Acta Materialia, 2011, 59, 5135-5145.

[51] S. Deville, *Freeze-casting of porous ceramics: A review of current achievements and issues*, Advanced Engineering Materials, 2008, 10, 155-169.

[52] U. G. K. Wegst, M. Schecter, A. E. Donius, and P. M. Hunger, *Biomaterials by freeze casting*, Philosophical Transactions of the Royal Society A, 2010, 368, 2099-2121.

[53] T. Fukasawa, Z. Y. Deng, M. Ando, T. Ohji, and Y. Goto, *Pore structure of porous ceramics synthesized from water-based slurry by freeze-dry process*, Journal of Materials Science, 2001, 36, 2523–2527.

[54] R. Chen, C. A. Wang, Y. Huang, L. Ma, and W. Lin, *Ceramics with special porous structures fabricated by freeze-gelcasting: using tert-butyl alcohol as a template*, Journal of the American Ceramic Society, 2007, 90, 3478–3484.

[55] E. Munch, E. Saiz, A. P. Tomsia, and S. Deville, *Architectural control of freeze-cast ceramics through additives and templating*, Journal of the American Ceramic Society, 2009, 92, 1534–1539.

[56] H. D. Jung, S. W. Yook, H. E. Kim, and Y. H. Koh, *Fabrication of titanium scaffolds with porosity and pore size gradients by sequential freeze casting*, Materials Letters, 2009, 63, 1545–1547.

[57] H. Schoof, J. Apel, I. Heschel, and G. Rau, *Control of pore structure and size in freeze dried collagen sponges*, Journal of Biomedical Materials Research, 2001, 58, 352–357.

[58] S. Deville, E. Saiz, and A. P. Tomsia, *Ice-templated porous alumina structures*, Acta Materialia, 2007, 55, 1965 – 1974.

[59] A. Lichtner, D. Roussel, and D. Jauffrès, C.L. Martin, R.K. Bordia, *Effect of macropore anisotropy on the mechanical response of hierarchically porous ceramics*, Journal of the American Ceramic Society, 2016, 99, 979–987.

[60] P. M. Hunger, A. E. Donious, and U. G. K. Wegst, *Structure-property-processing correlations in freeze-cast composite scaffolds*, Acta Biomaterialia, 2013, 9, 6338 – 6348.

[61] M.M. Porter, R. Imperio, M. Wen, M.A. Meyers, and J. McKittrick, *Bioinspired scaffolds with varying pore architectures and mechanical properties*, Advanced Functional Materials, 2014, 24, 1978–1987.

[62] S. Deville, *Ice templating, freeze casting: Beyond materials processing*, Journal of Materials Research, 2013, 28, 2202-2219.

[63] Y.M. Tan, O. Cervantes, S.W. Nam, J. D. Molitoris, and J.P. Hooper, *Dynamic fragmentation of cellular, ice-templated alumina scaffolds*, Journal of Applied Physics, 2016, 024901-1 – 024901-8.

[64] S. Deville, E. Saiz, and A.P. Tomsia, *Freeze casting of hydroxyapatite scaffolds for bone tissue engineering*, Biomaterials, 2006, 27, 5480–5489.

[65] A. Lichtner, D. Roussel, D. Jauffrès, C.L. Martin, and R.K. Bordia, *Effect of macropore anisotropy on the mechanical response of hierarchically porous ceramics*, Journal of the American Ceramic Society, 2016, 99, 979–987.

[66] T.L. Cable, and S.W. Sofie, *A symmetrical, planar SOFC design for NASA's high specific power density requirements*, Journal of Power Sources, 2007, 174, 221–227.

[67] Z. He, J. Liu, Y. Qiao, C.M. Li, and T.T.Y. Tan, *Architecture engineering of hierarchically porous chitosan/vacuum-stripped graphene scaffold as bioanode for high performance microbial fuel cell*, Nano Letters, 2012, 12, 4738−4741.

[68] P. Gannon, S. Sofie, M. Deibert, R. Smith, and V. Gorokhovsky, *Thin film YSZ coatings on functionally graded freeze cast NiO/YSZ SOFC anode supports*, Journal of Applied Electrochemistry, 2009, 39, 497–502.

[69] V. Naglieri, H.A. Bale, B. Gludovatz, A.P. Tomsia, and R.O. Ritchie, *On the development of ice-templated silicon carbide scaffolds for nature-inspired structural materials*, Acta Materialia, 2013, 61, 6948–6957.

[70] A. Ojuva, M. Järveläinen, M. Bauer, L. Keskinen, M. Valkonen, F. Akhtar, E. Levänenc, and L. Bergström, *Mechanical performance and CO_2 uptake of ion-exchanged zeolite A structured by freeze-casting*, Journal of the European Ceramic Society, 2015, 35, 2607–2618.

[71] S. Deville, S. Meille, and J. Seuba, *A meta-analysis of the mechanical properties of ice-templated ceramics and metals*, Science and Technology of Advanced Materials, 2015, 16, 043501-1–043501-15.

[72] J. Seuba, S. Deville, C. Guizard, and A.J. Stevenson, *Mechanical properties and failure behavior of unidirectional porous ceramics*, Scientific Reports, 2016, 6, 24326-1–24326-11.

[73] Q. Fu, M.N. Rahaman, F. Dogan, and B.S. Bal, *Freeze casting of porous hydroxyapatite scaffolds. II. Sintering, microstructure, and mechanical behavior*, Journal of Biomedical Materials Research Part B: Applied Biomaterials, 2008, 86B, 514–522.

[74] S. Deville, E. Maire, A. Lasalle, A. Bogner, C. Gauthier, J. Leloup, and C. Guizard, *Influence of particle size on ice nucleation and growth during the ice-templating process*, Journal of the American Ceramic Society, 2010, 93, 2507–2510.

[75] S. Deville, E. Maire, A. Lasalle, A. Bogner, C. Gauthier, J. Leloup, and C. Guizard, *In situ X-ray radiography and tomography observations of the solidification of aqueous alumina particle suspensions—part I: Initial instants*, Journal of the American Ceramic Society, 2009, 92, 2489–2496.

[76] R.N. Mohamed, *Sintering of ceramics*, CRC Press, Boca Raton, USA, 2007.

[77] S. Deville, E. Maire, G. Bernard-Granger, A. Lasalle, A. Bogner, C. Gauthier, J. Leloup, and C. Guizard, *Metastable and unstable cellular solidification of colloidal suspensions*, Nature Materials, 2009, 8, 966–972.

[78] S. Deville, and G. Bernard-Granger, *Influence of surface tension, osmotic pressure and pores morphology on the densification of ice-templated ceramics*, Journal of the European Ceramic Society, 2011, 31, 983–987.

VITA

Nikhil D. Dhavale was born in Dombivli, MH, INDIA on October 25th 1986. He graduated from University of Mumbai in 2008 with a Bachelor of Engineering degree in Mechanical Engineering. He has worked as an intern in the Ship Building department of Mazagon Dock Ltd. (a government of India undertaking) for two years. Following his undergraduate education, he was offered a fulltime job opportunity with AB Volvo group’s Volvo-Eicher Commercial Vehicles Limited, India. During his three and a half years of service, he has worked as a Supervisor in the Plant Maintenance and Quality Assurance Departments. To advance his academic and technical knowledge in the field of Aerospace engineering he joined the Master of Science program in Aerospace Engineering, at Embry-Riddle Aeronautical University, Daytona Beach, FL in the spring of 2012. He learned the basics of Aerospace Engineering during his time there, after which he moved on to Old Dominion University, Norfolk, VA to earn his Master of Science degree in Aerospace Engineering where, he gained advanced knowledge in the field of Aerospace structures and materials. Meanwhile, Nikhil has earned his Master of Business Administration in Management and Leadership from Webster University, St. Louis, MO. At ODU, he has worked closely with Dr. Dipankar Ghosh in his LEEM laboratory from summer 2015 to summer 2016 where he learned about ceramics and their processing in detail.

International journal publication and conference poster presentation:

D. Ghosh, **N. D. Dhavale**, M. Banda, H. Kang, *A comparison of microstructure and uniaxial compressive response of ice-templated alumina scaffolds fabricated from two different particle sizes,* Ceramics International (Volume 42, Issue 14, 1 November 2016, Pages 16138–16147) and 41st International Conference and Expo on Advanced Ceramics and Composites, Daytona Beach, FL (January 22-27, 2017) (Abstract submitted).